Title
Serine 421 is a crucial mediator of pathology in a mouse model of Huntington's disease

Author
Kratter, Ian

Publication Date
2013

Peer reviewed|Thesis/dissertation

Serine 421 is a Crucial Mediator of Pathology in a Mouse Model of Huntington's Disease

by

Ian H. Kratter

DISSERTATION

Submitted in partial satisfaction of the requirements for the degree of

DOCTOR OF PHILOSOPHY

in

Biomedical Sciences

in the

GRADUATE DIVISION

of the

Acknowledgements

In many ways I consider this section to be the most important part of my thesis, as so many people directly and indirectly have helped and supported me through my five years in the lab. Much of graduate school, regardless of the specifics of one's project, is about learning to think like a scientist. Ideally, scientific experiments are done in a metaphorical vacuum – we attempt to manipulate only a single variable and then examine its effect(s) so as to support or reject our hypothesis. Life in graduate school, on the other hand, is a very human pursuit that occurs in the real, hyperconnected 21st century world. While I have no doubt that I have grown tremendously as a scientist over the years, I strongly believe that I've grown even more as a person. I've had the opportunity to work with incredible role models, to learn self-reliance and perseverance in the face of seemingly-constant failure, and to refine my ability to navigate a complex and often frustrating world without sacrificing my values or losing the pleasure I derive from simply being curious. Importantly, I've learned more about my own limits and weaknesses, and I've worked on both addressing them and improving my strategies for compensating for them. Just as crucially, I've realized how unsatisfied I feel professionally regardless of success without appropriate prioritization and maintenance of the important personal relationships and extracurricular activities that make me feel whole.

I must begin by thanking my family, especially my parents. Your love and support throughout a process that you minimally understand has been incredible. I cannot imagine how frustrating it must have been to hear so often that lab work was coming along "slowly" and that I am "maybe" getting closer to finishing. Thank you for your patience during this time and, more importantly, thank you for instilling the kind of values

in me that led to this amazing opportunity to receive world-class training and to make a small contribution to medical science. Also, many thanks to my sister, Nina, and brother, Ricky. Your love and constant ability to lift my spirits and make me laugh have been priceless. Nina, it has been simply fantastic having you live in the same city. Ricky, I will never forget our Outside Lands weekends that invariably refreshed my mind and my spirit.

I want to thank my fiancée, Chelsey, for the numerous ways that she brings joy to my life and for the patience she exudes in handling my quirks. I truly cannot imagine having finished a PhD without having had her with me almost every step of the way. From the incredible weekend trips we have taken to coming home after a long and frustrating day to a smile, hug, and warm dinner, you have been there for me more times than I can possibly count. The effort you have made without scientific training to understand my work and my daily experimental life is one of the many truly special things about you. No example is better than the time you memorized the entire protocol for a western blot(ter), which is truly one of the sweetest things anyone has ever done for me.

Enormous thanks are also due to my boss and mentor, Steve Finkbeiner. I cannot put into words how much respect and admiration I have for you. When I first interviewed for the MD/PhD program at UCSF, Steve was my final interview of the entire two-day long process. I distinctly remember walking out of that interview and calling up my dad as I walked towards the shuttle. He asked me how the interviews went, and I told him that I just might have spoken to the smartest person I had ever met. Having been at UCSF now for 7 years, I have had the good fortune to meet an incredible number of brilliant faculty, professionals, and colleagues. Still, I have met precious few who can combine diverse interests, towering intellect, indefatigable work ethic, passion for their work, a

commitment to mentorship, and an incredibly generous and positive spirit the way Steve does. Trying to list the things that Steve has taught me over the years (and still will teach me in the future) would be impossible to do, but as I reflect back on recent feedback I gave to a first year graduate student on a scientific proposal, I realized just how much of what I was saying was a repackaging of something Steve had once told me. Truly, in this case at least, imitation is the sincerest form of flattery.

Steve has had and continues to have a number of truly incredible people in his lab, and I am deeply appreciative for the opportunity he gave me and the patience he demonstrated during my first few clueless years of graduate school. Steve's time is his most precious resource, and I am embarrassed by how much of it I used up being clueless and talking about what in retrospect was nonsense. But he always indulged me and had me do things like write emails to collaborators that he could have done better and faster himself, all for the sake of teaching me how to be an independent scientist. I hope that wherever my career takes me, I can one day emulate these values and traits to the best of my abilities.

While speaking of professors, I'd like to thank the other members of my thesis committee, Tony Wynshaw-Boris and Paul Muchowski. Their feedback, insight, and experience have helped improve my project, and both have helped me setup intriguing ongoing collaborations. Kelley Nelson, Lisa Magargal, Monique Piazza, Jana Toutolmin, and Catherine Norton also deserve a huge heaping of thanks for keeping the lab, graduate, and MST programs running like well-oiled machines.

The members of the Finkbeiner lab make it a truly special place to do science, and I want to thank all of them past and present for their generosity, kindness, and friendship.

I have had the good fortune to spend the last 5 years looking forward to the company of the people around me. In no particular order, Montse, Erica, Eva, Sami, Mike, Julia M., Julia K., Carol, Hong Joo, Andrey, Maya, Matt, Kelly, Lisa, Rebecca, Amanda, Arpana, Adam, Ana, Tina, Punita, and Sean: it has been a pleasure working with you and learning from you. The same goes for Earl Rutenber and Sue-Ann Mok, both of whom I consider to be pseudo lab members.

There are a couple of lab members that I want to highlight individually because they have meant so much to me during my time here. Aaron Daub and Hengameh Zahed have been my partners in crime, so to speak, for almost the entire time. Aaron, your glowing optimism and incredible kindness inspire me to be a better person. Hengameh, you have taught me wonderful lessons in thorough scholarly research and about the importance of self-reliance and internal resilience. I was already quite friendly with them both before they joined the lab, and so when they each independently chose to join I felt incredibly lucky. I am not sure how many people get to work with two of their best friends day after day, but it cannot be too many. It has been an honor to share the many late nights, long weekends, and failed experiments with them, not to mention soccer games, Tahoe trips, and jumps out of an airplane. In addition, Hengameh has made significant contributions to the work presented in this thesis. In short, I think it is unlikely that I would be completing this thesis at this time without their presence in the lab and in my life. You both are like family to me.

Another person who deserves extra special recognition is Jason Miller. Jason was a senior graduate student when I joined the lab and quickly became a mentor and role model to me. I was immediately struck by his unique mix of brilliance, compassion, and modesty. He is one of those rare people like Steve that has been blessed with incredible

innate talent but has also worked extremely hard to harness that talent in a powerful but selfless way. Jason, like me, also has a sometimes inelegant sense of humor, and this probably had a lot to do with why we quickly became really close friends. Jason never fails to motivate me to work harder and smarter in the lab, clinic, and gym. His future potential is limitless, and I am excited to observe and play a small part in the next chapters of his life. Chelsey, too, was quickly awed by Jason's unique blend of savvy and spirit, and we both are excited and honored that he has agreed to officiate our wedding.

My friends outside the lab also deserve a special 'thank you'. Ariel, Aaron, Joel, Tania, Jason, and David – to name a few – although you were often not close in proximity, your friendship and support have been invaluable to me and helped keep me going through the difficult times. You all inspire me with your unique attributes, and I hope I will be able to give back some fraction of what your friendship has meant to me.

Contribution of Others in Work Presented

Much of the data presented in this thesis is the result of fruitful collaborations for which I am grateful. The neuropathology and electron microscopy was performed by Dr. Eliezer Masliah. The immunohistochemistry revealing mutant Huntingtin inclusion bodies and BDNF levels was performed by Dr. Alexander Osmand. The work in St14A cells was performed by Dr. Joan Steffan using Htt-N480 constructs from Drs. Frédéric Saudou and Sandrine Humbert. Purification of the BAC DNA for pronuclear injection was performed with advice from Drs. Xiaofeng Gu and X. William Yang and with assistance from Dr. Andrey Tsvetkov. The Htt-N586 constructs were created in collaboration with Hengameh Zahed and Aaron Daub. The S421 phosphospecific antibodies were created with Hengameh Zahed, who also assisted in multiple other ways. The subcellular localization of Htt-N586 constructs in N2a cells was performed by Dr. Danny Hatters.

Part of the text of the discussion and the accompanying figure were originally published by Kratter, I.H. and Finkbeiner, S. (*Neuron*. 2010 Sep 23;67(6):897-9. doi: 10.1016/j.neuron.2010.09.012.).

I would also like to acknowledge continuing collaborations with Drs. Matthew Campioni, Kelly Haston, Sue-Ann Mok, Danny Hatters, Niels Skotte, and Michael Hayden. The associated work does not appear in this thesis but is very much a part of our ongoing investigation of the significance of Htt-S421.

Abstract

Serine 421 is a crucial mediator of pathology in a mouse model of Huntington's disease

By

Ian H. Kratter

Huntington's disease (HD) is a progressive, adult-onset neurodegenerative disease without cure or disease-modifying therapy caused by a polyglutamine (polyQ) expansion in the N-terminal region of the protein huntingtin (Htt). Pathological hallmarks of HD include selective neuron loss and protein aggregation, but the etiology remains unclear. Htt has a highly conserved phosphorylation site at serine 421 (S421-P), and basal levels of S421-P in the brain are inversely correlated to tissue vulnerability. Further, prior work found that S421-P diminishes the toxicity of mutant Htt fragments. However, whether S421-P affects the toxicity of mutant Htt *in vivo* remains unknown. To determine the role of S421-P in mutant Htt-induced neurodegeneration *in vivo*, we mutated the human Htt gene within a bacterial artificial chromosome (BAC), previously used to create the BACHD mouse model of HD, to express either an aspartic acid or alanine at position 421 to mimic tonic phosphorylation (S421D) or to prevent phosphorylation (S421A), respectively. We used the mutated BACs to generate new lines of transgenic mice and compared their behavior and neuropathology to the unmodified HD mice and wildtype controls. We found that S421D mice that expressed Htt in the cortex at levels similar to the original BACHD model had significantly less motor and psychiatric-like dysfunction

than BACHD mice at multiple time points. Further, 12-month-old BACHD but not S421D mice showed evidence of striatal neurodegeneration when compared to wildtype controls despite a similar load of Htt inclusion bodies. S421A mutants with considerably lower mutant Htt expression demonstrated a mild behavioral phenotype similar to that reported in the BACHD-L (low expressing) line. Surprisingly, while S421D mice had similar levels as BACHD mice of both Htt mRNA and soluble protein in the cortex, they had relatively decreased steady-state levels of protein but not mRNA in the striatum. Biochemical analyses confirmed that S421D decreased the steady-state levels of soluble Htt in a striatal cell line and suggested that this occurs via increased Htt flux through the proteasome. In sum, our work suggests that S421 phosphorylation significantly ameliorates mutant Htt toxicity in mice and thereby validates phosphorylation at S421 as a therapeutic target in HD.

Table of Contents

List of Tables

List of Figures

Chapter 1: A brief introduction to Huntington's disease

Huntington's disease (HD) is a progressive, devastating neurodegenerative disorder without any cure or disease-altering treatment. HD patients present clinically with any combination of chorea, dystonia, incoordination, cognitive impairments, personality changes, and mood disturbances, invariably culminating in early death. While the prevalence varies with geography, 5-7 affected individuals per 100,000 is an accurate general estimate (1, 2). HD is inherited in an autosomal dominant fashion, and a collaborative hunt for a genetic cause identified *huntingtin* (*htt*) as the gene whose mutation causes HD (3). *Htt* codes for a widely-expressed 350 kDa protein with no overall homology to any other known protein and which contains a polyglutamine (polyQ) repeat stretch of variable length near its N-terminus. Expansion of this stretch beyond 36 repeats may or may not cause disease, but expansion beyond 40 repeats guarantees disease if the patient lives long enough. Additionally, the length of the polyQ repeat stretch is inversely proportional to the age of disease onset. Among the most common HD alleles (40-50 repeats), 50-70% of the age of onset is explained by the length of the polyQ stretch, implying that the remainder is explained by genetic modifiers and environmental factors (4).

Pathological inspection of the HD brain reveals profound atrophy and eventual cell death of the medium spiny neurons (MSNs) of the striatum (5). Deep layers of the cortex, the CA1 region of the hippocampus, and many other regions of the brain are also impacted as the disease progresses, though other regions such as the cerebellum are relatively spared. Neurons with abnormal nuclear and/or cytoplasmic protein inclusions consisting

in part of aggregated Htt and ubiquitin are a pathological hallmark of HD (5), but they do not seem to underlie the disease (6).

Htt is expressed in all human cells, but the mechanisms causing a selective neurodegenerative disease in the context of polyQ expansion remain obscure. PolyQ expansion causes Htt to misfold, which is thought to confer a toxic gain of function (GOF) (7). Indeed, a myriad of pathogenic mechanisms such as alterations in protein binding partners (8), NMDA signaling (9), and global protein homeostasis (10) have been reported.

While a GOF is consistent with the autosomal dominant inheritance, there is also evidence to support a contribution to pathogenesis from loss of function (LOF) of the wildtype (WT) allele (11). For example, the neurotrophin BDNF is a crucial extracellular trophic factor and signaling molecule implicated in core brain processes and neuronal survival (12), but the striatum produces little of its own BDNF and instead crucially depends on its delivery from other brain regions, particularly the cortex (13-15). Apparently, WT Htt facilitates a de-repression of *BDNF* transcription but polyQ-expanded Htt does not (16), and several studies have implicated such a reduction of BDNF at the transcriptional level as an important contributor to HD pathogenesis (17-19). Additionally, WT Htt has been implicated in a multitude of other cellular processes, including intracellular signaling, metabolism, gene expression, and intracellular transport, but its precise native function remains unknown (20, 21).

Although the molecular details of HD remain puzzling, therapeutic intervention may not require a complete understanding of its etiology. One potentially promising approach is to combat the inherent toxicity of the mutant protein. This could involve directly targeting the polyQ expansion. In fact, HD is one of at least nine genetic diseases caused by an abnormal expansion of a polyQ stretch, highlighting the inherent toxicity of polyQ-mediated protein misfolding in disease pathogenesis (22). However, there may be other approaches worth pursuing. For example, increasing evidence points to the crucial role that host protein context plays in pathogenesis. Post-translational modifications (PTMs), in particular, greatly influence the toxicity of several different mutant polyQ proteins, including Htt (23, 24), and might be easier to target pharmacologically. Furthermore, several PTMs localized to the N-terminal 17 amino acids of Htt are known to modulate toxicity of the mutant protein (25-30). These residues, immediately preceding the polyQ stretch, are well positioned to alter the expansion's propensity to cause protein misfolding via both direct and indirect means. However, other Htt PTMs farther away from the polyQ repeat region by primary sequence also can modify mutant Htt (mHtt) toxicity (31-41).

Serine 421 of Htt is a consensus Akt phosphorylation site (31) and also can be phosphorylated by the serum- and glucocorticoid-induced kinase (SGK) (42). In a primary striatal neuron model of HD (43), the toxicity of an overexpressed Htt-N480-68Q fragment is eliminated by enhancing S421 phosphorylation (S421-P). Mimicking tonic phosphorylation with a serine-to-aspartic acid mutation (S421D) similarly eliminates mutant Htt toxicity. Conversely, a serine-to-alanine mutation (S421A) in Htt that prevents phosphorylation preserves toxicity (31). Further, genetic and pharmacological inhibition of calcineurin (CaN), a putative S421 phosphatase, reduces the toxicity of lentivirus-mediated expression of a Htt fragment in rat striatum (44). Studies of S421-P in cell

culture systems suggest that it influences Htt's proposed regulatory role in vesicular trafficking (45-47) and is associated with a decrease in both buildup of nuclear Htt fragments (48) and NMDA-mediated excitotoxicity (49).

Importantly, polyQ expansion causes a decrease in the proportion of Htt phosphorylated at S421 (44, 50), and the degree of phosphorylation in specific brain tissues correlates inversely with susceptibility to degeneration in HD. Specifically, the cerebellum, which is largely spared in HD, has the highest proportion of S421-P, while the striatum, devastated in HD, has the lowest. Cortical S421-P levels lie between those tissue types, consistent with its relative vulnerability to the disease (50). These findings suggest that S421-P modulates Htt toxicity and could influence the tissue-specific nature of HD. There are important caveats to note in the previous studies of S421-P, however, and their impact on the conclusions drawn from that work must be considered. For example, overexpression of an N-terminal fragment of Htt might not represent an accurate model of HD due to the non-physiological expression levels achieved with transient transfection and the somewhat arbitrary nature of the N-terminal truncation and subsequent loss of the majority of the Htt protein. The use of virus to introduce a fragment of Htt into rat striatum raises these same concerns, in addition to the possibility of the induction of inflammatory changes that might impact the neurodegenerative process. Also, none of these studies consider a potential developmental aspect to HD pathogenesis caused by embryonic expression of mHtt, nor can they perform detailed circuit- and cell-specificity analyses that might be altered by S421-P. Therefore, it remains unknown whether S421-P affects the toxicity of full-length mHtt (fl-mHtt) *in vivo*. This thesis reports our attempt to address this question so as to determine whether S421-P should be pursued further as a therapeutic target.

This project necessitates an appropriate *in vivo* model of HD, and the monogenic nature of HD has allowed the development of a wide variety of murine models of the disease (51). The most aggressive models are based on the transgenic overexpression of an exon1 fragment of Htt (52). While the rapid onset of pathology has made these mice quite useful for pre-clinical drug testing, there remains substantial debate about whether or not expression of exon1 alone is a sufficiently representative model of HD. Further, exon1 does not contain S421, precluding our use of these models to address our question.

On the other hand, genetically precise knock-in mouse models where endogenous mouse *Htt* is altered to express an expanded polyQ repeat stretch also exist. However, there are potentially important differences between the mouse and human forms of Htt, which might account at least partially for the modest phenotypes seen in these mice. For instance, the recently reported 200Q knock-in mice do not demonstrate behavioral dysfunction until at least 5 months of age in the homozygous animals or almost one year of age in the heterozygotes, nor is there any frank neurodegeneration (53). These drawbacks necessitate larger cohorts and extended aging of the animals, a particularly problematic logistical issue when two different mutations (i.e., S421D and S421A) are to be compared to both HD and WT mice.

An alternative approach has been to use a yeast or bacterial artificial chromosome (YAC/BAC) to express full-length human *Htt* under the control of its endogenous regulatory machinery (54, 55). These mice demonstrate early (2 months of age) and robust motor deficits as well as progressive neuropathology, making them a good choice for hypothesis testing and various ‘omics approaches. Thus, BACHD mice are an appropriate model for our studies.

In chapter 2, we address whether S421-P affects mutant Htt toxicity *in vivo* by creating and characterizing models of BACHD mice with mutations at S421. We demonstrate that a phosphomimetic mutation at that site ameliorates multiple behavioral and histopathological phenotypes evoked by the overexpression of fl-mHtt. We also report that S421D decreases steady-state levels of soluble Htt protein, presumably by increasing Htt turnover. In chapter 3, we use BACHD mice to examine the reported transcriptional dysfunction caused by Htt LOF, as exemplified by altered BDNF transcription. We determine that BDNF transcriptional dysfunction is not in fact a significant cause of disease in the BACHD model. In chapter 4, we discuss the implications of these findings.

Chapter 2: Serine 421 is a crucial mediator of pathology in a mouse model of Huntington's disease

Introduction

As previously discussed, increasing evidence points to the crucial role that host protein context plays in the toxicity of disease-associated polyQ expansions. PTMs, in particular, greatly influence the toxicity of several different mutant polyQ proteins, including Htt (23, 24). Specifically, several PTMs localized to the N-terminal 17 amino acids of Htt modulate toxicity of the mutant protein (25-30). These residues, immediately preceding the polyQ stretch, are well positioned to alter the expansion's propensity to cause protein misfolding via both direct and indirect means. However, other Htt PTMs farther away from the polyQ repeat region by primary sequence also have been reported to modify mHtt toxicity (31-41).

Serine 421 of Htt is a consensus Akt phosphorylation site (31) and also can be phosphorylated by the serum- and glucocorticoid-induced kinase (SGK) (42). In a primary striatal neuron model of HD (43), the toxicity of an overexpressed Htt-N480-68Q fragment is eliminated by enhancing S421-P. Mimicking tonic phosphorylation with a serine-to-aspartic acid mutation (S421D) similarly eliminates mutant Htt toxicity. Conversely, a serine-to-alanine mutation (S421A) in Htt that prevents phosphorylation preserves toxicity (31). Further, genetic and pharmacological inhibition of calcineurin (CaN), a putative S421 phosphatase, reduces the toxicity of lentivirus-mediated expression of a Htt fragment in rat striatum (44). Studies of S421-P in cell culture systems suggest that it influences Htt's proposed regulatory role in vesicular trafficking

(45-47) and is associated with a decrease in both buildup of nuclear Htt fragments (48) and NMDA-mediated excitotoxicity (49).

Importantly, polyQ expansion causes a decrease in the proportion of Htt phosphorylated at S421 (44, 50), and the degree of phosphorylation in specific brain tissues correlates inversely with susceptibility to degeneration in HD. Specifically, the cerebellum, which is largely spared in HD, has the highest proportion of S421-P, while the striatum, devastated in HD, has the lowest. Cortical S421-P levels lie between those tissue types, consistent with its relative vulnerability to the disease (50). These findings suggest that S421-P modulates Htt toxicity and could influence the tissue-specific nature of HD. There are important caveats to note in the previous studies of S421-P, however, and their impact on the conclusions drawn from that work must be considered. For example, overexpression of an N-terminal fragment of Htt might not represent an accurate model of HD due to the non-physiological expression levels achieved with transient transfection and the somewhat arbitrary nature of the N-terminal truncation and subsequent loss of the majority of the Htt protein. The use of virus to introduce a fragment of Htt into rat striatum raises these same concerns, in addition to the possibility of the induction of inflammatory changes that might impact the neurodegenerative process. Also, none of these studies consider a potential developmental aspect to HD pathogenesis caused by embryonic expression of mHtt, nor can they perform detailed circuit- and cell-specificity analyses that might be altered by S421-P. Therefore, it remains unknown whether S421-P affects the toxicity of full-length mHtt (fl-mHtt) *in vivo*.

To determine the role of S421-P in fl-mHtt-induced neurodegeneration *in vivo*, we altered the mutant human Htt gene within the bacterial artificial chromosome (BAC) previously used to create the BACHD mouse model of HD (55) to express either S421D

or S421A. We show that S421D but not S421A strongly ameliorates mHtt-induced behavioral dysfunction and neurodegeneration. We present evidence suggesting that S421D decreases steady-state levels of striatal mHtt, potentially by increasing turnover of mHtt through the proteasome. Thus, our work suggests that phosphorylation at S421 significantly ameliorates mHtt toxicity in mice and thereby validates it as a therapeutic target in HD.

Results

Generating and characterizing BAC transgenic mice expressing full-length mutant Huntingtin with mutation at phosphorylation site S421

To study the role of Htt-S421-P in a mammalian model system, we utilized the BACHD mouse model of HD. BACHD mice express fl-mHtt with a pathogenic 97Q repeat stretch under the control of its endogenous promoter. As they age, these mice show robust behavioral and histopathological phenotypes (27, 55).

First, we confirmed that Htt-S421 is phosphorylated in BACHD mice by generating affinity-purified S421-phosphospecific antibodies (31) (Fig. 1a). Immunoblotting of BACHD soluble brain lysates with our phosphospecific antibodies revealed a weak S421-P signal not observed in WT controls (Fig. 1b). This reduced level of S421-P is consistent with previous reports from cell and mouse models of HD showing that the proportion of S421-P Htt is significantly decreased in the context of the mutant polyQ expansion (44, 50).

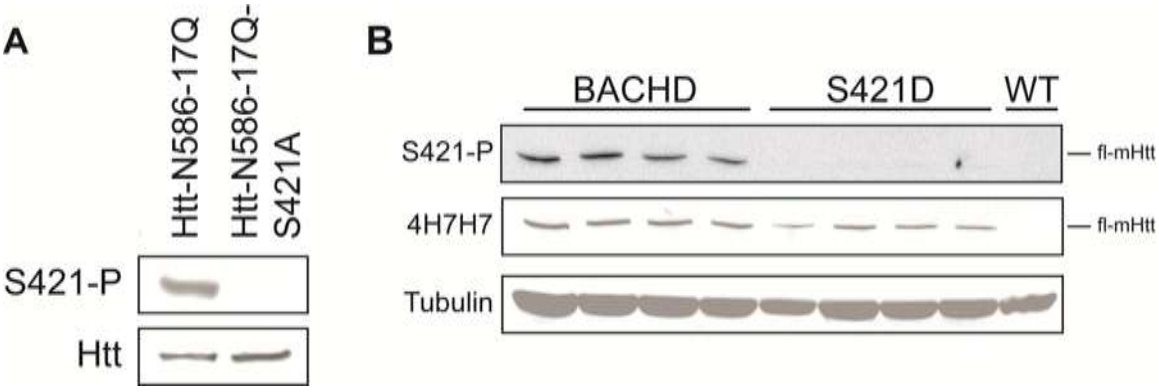

Figure 1. Full-length mutant huntingtin is phosphorylated at S421 in BACHD brain.

(A) Western blot of lysates from HEK293 cells transfected with Htt-N586-17Q or Htt-N586-17Q-S421A, using affinity-purified S421-P phosphospecific antibodies confirms their phospho-specificity. Blots were also probed with an anti-Htt antibody (mAb 2166) as a control.

(B) Western blot of striatal lysates from BACHD, S421D, or WT controls reveals that BACHD brains contain fl-mHtt phosphorylated at S421-P. As expected, the phospho-specific antibodies do not demonstrate immunoreactivity to the S421D lysate, confirming the specificity of BAC recombineering. Blots were also probed with anti-polyQ monoclonal antibody 4H7H7 and anti-γ-tubulin as controls.

We next sought to determine the relevance of S421-P to mHtt-induced neurodegeneration *in vivo.* We obtained the BAC used to generate the BACHD model, and we performed two parallel versions of Red/ET triple recombination, followed by FLP recombination to remove the selectable marker (Fig. 2a, b). The mutated BACs express either an aspartic acid or alanine at position 421 (Fig. 3a), as these mutations have commonly been used to mimic tonic phosphorylation (S→D) or prevent phosphorylation (S→A), respectively. We verified successful recombineering by PCR amplification of the local region followed by sequencing. We also sequenced the 5' and 3' ends of the Htt gene to confirm that the 97 mixed CAA-CAG codons encoding the expanded polyQ repeat were unaltered and that no other unintended mutations occurred. The structural

A

exon9

ACCTGTGTTTCTCTGTTTCTAGGTTTATGAACTGACGTTACATCATACACAGCACCAAGACCACAATGTTGTGACCGGAG
CCCTGGAGCTGTTGCAGCAGCTCTTCAGAACGCCTCCACCCGAGCTTCTGCAAACCCTGACCGCAGTCGGGGGCATTGGG

S495A: change AGT to GCT
S495D: change AGT to GAT

CAGCTCACCGCTGCTAAGGAGGAGTCTGGTGGCCGAAGCCGTAGTGGGAGTATTGTGGAACTTATAGGCAAGTTATTAGC
AAGGTCTACTCTTACAATTAACTTTGCAGTAATACTAGTTACACTCTATTGATTATGGGCCTGCCCTGTGCTAAGCAGTC
TGCATTCCATCTTCCTTGCCAAAACTTATAATACAAATTTCATCTTTATTTTATAAATAGGGGAGTTGGGCTGGGTGTGG

P169-check3

TGGCTCACGCCTGTAATTTCAGCACTTTGGAAGGATCGCTTCAGCCCAGGAGTTTGAGACAACCTGGCCAAGTGAGACCC

P169-check4

TGTCTCTACAAAAAAAAAAAAAAAAAAAAAATTAGCTGGGCATGGTGGCACATGCCTGTAGTCCCAGCTGCTTTGGAGGC

insert FRT-neo-FRT

TGAGGTGGTAGGATTGCTTAAGCCCAAGAGGTTGAGGCTGCAGTGAATCTTGATGGCAGCTGCACTGAGCCTGGTGACAG
AGCAAGATGCTGTCTCAAAATAAATTTAAAAATAAAATAAGAGAATTAAAGTTTAGCAGGTTGGGTGGCAAAATGAGGCC

B

exon9

ACCTGTGTTTCTCTGTTTCTAGGTTTATGAACTGACGTTACATCATACACAGCACCAAGACCACAATGTTGTGACCGGAG
CCCTGGAGCTGTTGCAGCAGCTCTTCAGAACGCCTCCACCCGAGCTTCTGCAAACCCTGACCGCAGTCGGGGGCATTGGG
CAGCTCACCGCTGCTAAGGAGGAGTCTGGTGGCCGAAGCCGTAGTGGGGCTATTGTGGAACTTATAGGCAAGTTATTAGC
AAGGTCTACTCTTACAATTAACTTTGCAGTAATACTAGTTACACTCTATTGATTATGGGCCTGCCCTGTGCTAAGCAGTC
TGCATTCCATCTTCCTTGCCAAAACTTATAATACAAATTTCATCTTTATTTTATAAATAGGGGAGTTGGGCTGGGTGTGG

P169-check3

TGGCTCACGCCTGTAATTTCAGCACTTTGGAAGGATCGCTTCAGCCCAGGAGTTTGAGACAACCTGGCCAAGTGAGACCC

P169 check4

TGTCTCTACAAAAAAAAAAAAAAAAAAAAAATTAGCTGGGCATGGTGGCACATGCCTGTAGTCCCAGCTGCTTTGGAGGC

FRT foot print primer binding site

TGAGGTGGTAGGATTGCTTAAGCCCAAGAGGTTGAGGAAGTTCCTATTCTCTAGAAAGTATAGGAACTTCCTCGAGCCCT
ATAGTGAGTCGTATTAGCTGCAGTGAATCTTGATGGCAGCTGCACTGAGCCTGGTGACAGAGCAAGATGCTGTCTCAAAA
TAAATTTAAAAATAAAATAAGAGAATTAAAGTTTAGCAGGTTGGGTGGCAAAATGAGGCCACACATTTAAAGCCCCTCCT

C

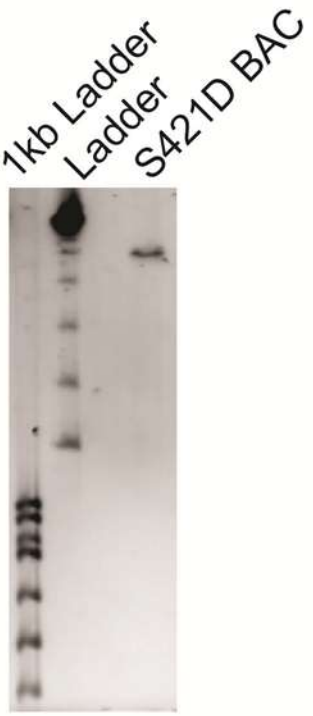

Figure 2. Mutation and purification of S421D and S421A BACs for pro-nuclear microinjection.

(A) The *HTT* genomic locus before manipulation by Red/ET recombination as predicted on the original mutant version of BAC clone RP11-866L6. Exon9 containing S421 is marked in grey and flanking sequences are in black. The codon to be mutated and the insertion position of FRT-PGK-gb2-*neo/km*-FRT selection cassette are both emboldened. Locations of control primers used for PCR are also indicated. Note that S495 refers to S421 in the context of the 97Q repeat and conventional Htt sequence nomenclature.

(B) The *HTT* genomic locus after manipulation by Red/ET. The introduced point mutation S421A (S421D not shown) in exon9 of *HTT* locus is shown in bold. The remaining FRT-site after removal of FRT-PGK-gb2-*neo/km*-FRT cassette is grey and bolded. The primer binding site used for amplification of the kanamycin selection cassette is indicated in addition to the primers used for PCR.

(C) The cesium chloride purification method was used to purify S421D and S421A BACs, followed by linearization with PI-Sce-I. Pulsed-field gel electrophoresis was used to confirm that the BACs (S421A not shown) were intact and free of degraded BAC DNA fragments prior to pro-nuclear microinjection to generate transgenic founders.

integrities of the BACs were confirmed by pulsed-field gel electrophoresis. Finally, purified and linearized BAC DNA (Fig. 2c) was microinjected into FvB/N pro-nuclei to generate transgenic founders.

Seven founders with the BACHD-S421D transgene and two with the BACHD-S421A transgene (referred to herein as ‘S421D’ and ‘S421A’, respectively) were obtained. One S421D line and one S421A line expressed fl-mHtt at levels sufficient for meaningful analysis (see below). To control for genetic background, these two lines were expanded by breeding with FvB/NJ WT mice, the same inbred strain used to characterize the

original BACHD mice. Again, the transgene regions coding for mHtt exon1, the region around S421, and a portion of the 3' UTR were PCR-amplified and sequenced to confirm proper incorporation of the entire gene and S421 mutation without changes in the polyQ repeat length. We also confirmed the specificity of the mutations by immunoblotting brain lysates from the mutant mice with our S421 phosphospecific antibodies. As expected and as shown with N-terminal fragments of Htt (31), the phosphospecific antibodies did not recognize fl-mHtt with S421D or S421A mutation (Fig. 1b).

To characterize these mice, we analyzed fl-mHtt protein levels in the F1 progeny of the founder lines. Levels of fl-mHtt protein are generally directly proportional to their toxicity (55-57). Thus, to make the most meaningful comparisons, we looked for lines that expressed mHtt at levels similar to BACHD mice. We first used western blots to evaluate steady-state levels of soluble fl-mHtt levels in cortical lysates from 2-month-old mice. Because all lines have the same polyQ-repeat length, we used the mouse monoclonal antibody 4H7H7, which selectively recognizes pathogenic polyQ stretches (27). To increase the accuracy and dynamic range of the quantifications, we used near-infrared fluorescence for signal detection. One line of hemizygous S421D mice expressed fl-mHtt protein at levels similar to the original BACHD model (Fig. 3b, c). We confirmed this finding with 1C2, another mouse monoclonal antibody that recognizes mutant polyQ stretches (Fig. 4). We also analyzed levels of cortical mHtt transcript by quantitative reverse-transcriptase (qRT)-PCR. As observed at the protein level, S421D mice had approximately equivalent levels of mHtt mRNA as did BACHD mice (Fig. 3d).

We performed a similar analysis for the S421A mutant mice. One hemizygous line expressed approximately 45% of the fl-mHtt protein of BACHD mice (Fig. 3b, c). Levels of transcript were also consistent with this determination (Fig. 3d). Although these

significantly lower levels of fl-mHtt preclude a direct comparison of S421A and BACHD mice, mHtt expression levels were quite similar to the previously described lower-expressing BACHD-L line (Fig. 4) (55). Accordingly, S421A mice would be expected to show impaired motor coordination on the accelerating rotarod compared to WT littermate controls by 6 months of age, as do the BACHD-L mice. Thus, the S421A line has sufficient levels of expression to control for any non-specific effects of mutation at S421.

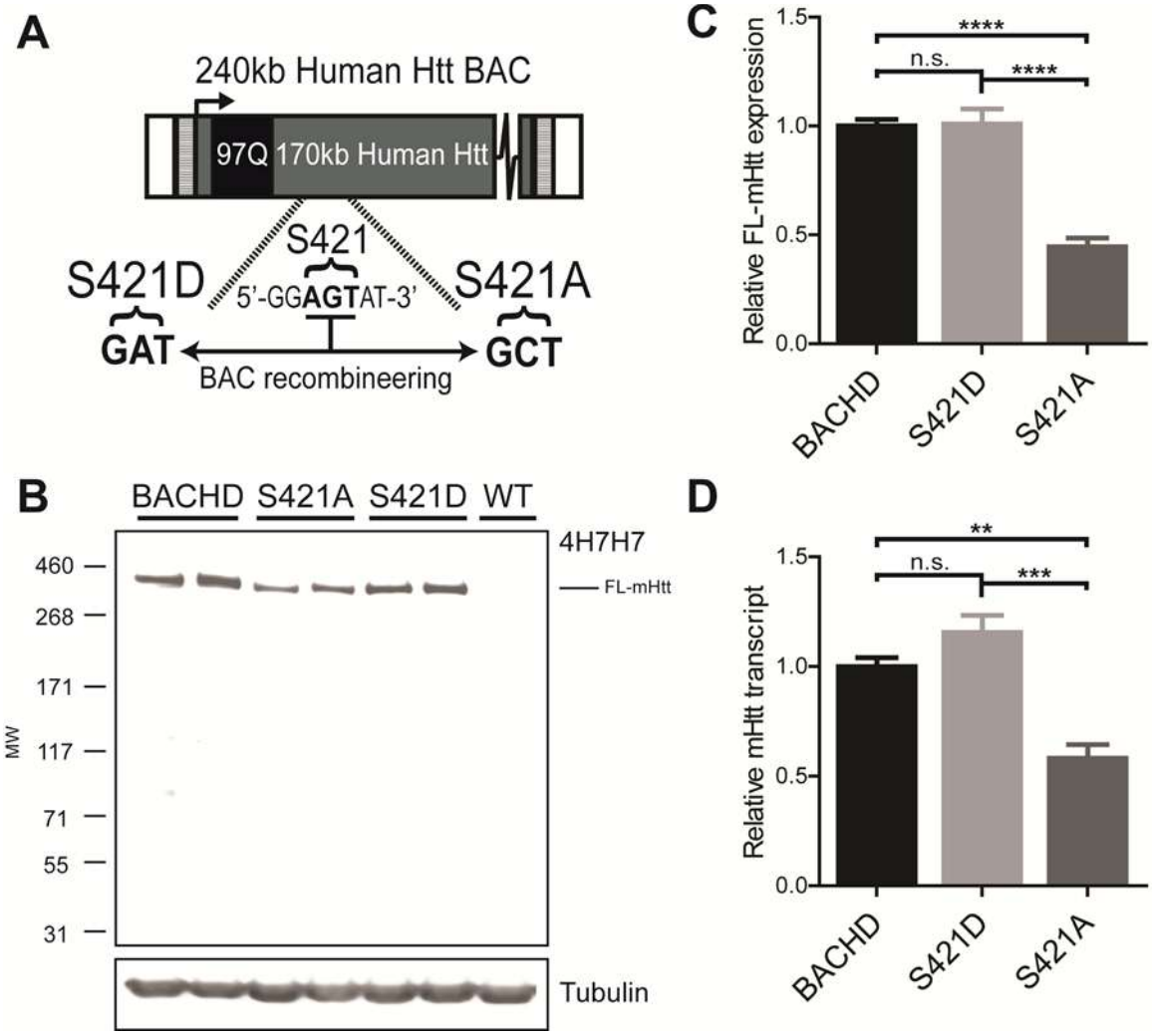

Figure 3. Generation and characterization of the phosphomimetic (S421D) and

phosphoresistant (S421A) BACHD transgenic mice.

(A) Schematic of the recombineered BAC cassette, in which S421D or S421A mutations within the original BACHD construct were generated.

(B) Representative western blot demonstrating expression levels of soluble fl-mHtt from cortical lysates of two-month-old BACHD, S421D, and S421A mice. The blot was probed with anti-expanded polyQ monoclonal antibody 4H7H7 and anti-γ-tubulin as a loading control.

(C) Quantification of expression levels of soluble fl-mHtt from cortical lysates of two-month-old BACHD, S421D, and S421A mice. Values are based on the mean of three independent 4H7H7 blots each with lysates from at least 3 mice per line compared across different blots by normalization to BACHD samples. Each value was first normalized for input by using the anti-γ-tubulin control. One-way ANOVA analysis reveals that there is a significant difference between the three lines ($F = 36.71$, $p < 0.0001$). Post-hoc Bonferroni analysis indicates that the fl-mHtt expression of the S421A line is significantly different from those of the BACHD ($p < 0.0001$) and S421D lines ($p < 0.0001$), whereas the BACHD and S421D mice express fl-mHtt at similar levels (n.s.).

(D) Quantification of the levels of cortical mHtt transcript in BACHD, S421D, and S421A mice by reverse-transcriptase qRT-PCR. The results are from four independent samples per transgenic line, each run in quadruplicate. Values are normalized to BACHD mice and are expressed in arbitrary units (au). One-way ANOVA analysis reveals significant differences ($F = 51.8$, $p < 0.0001$). Post-hoc Bonferroni analysis indicates that fl-mHtt expression in S421A mice is significantly lower than BACHD ($p < 0.0001$) and S421D lines ($p < 0.0001$), whereas the BACHD and S421D lines express at similar levels (n.s.).

****$p < 0.0001$; ***$p < 0.001$; **$p < 0.01$; n.s. = not significant.

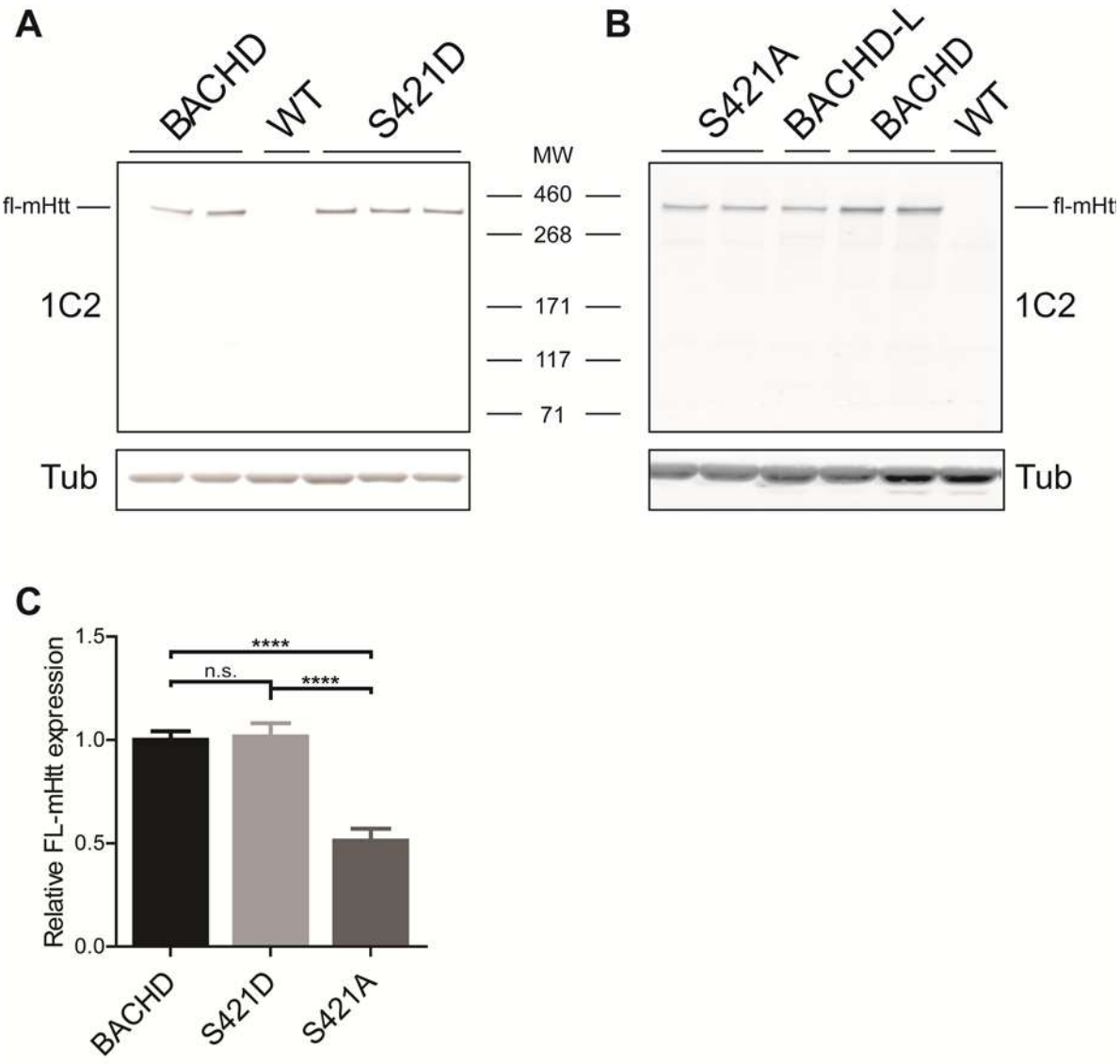

Figure 4. Additional biochemical characterization of full-length mutant Htt levels in S421D and S421A lines.

(A) Representative western blot demonstrating expression levels of soluble fl-mHtt from cortical lysates of BACHD and S421D mice. The blot was probed with mAb 1C2 and anti-γ-tubulin as a loading control.

(B) Representative western blot demonstrating expression levels of soluble fl-mHtt from cortical lysates of S421A and BACHD mice as well as from previously generated cortical lysate from

a BACHD-L mouse. S421A mice express the transgene at levels comparable to BACHD-L mice, implying that a phenotype should be detected on the accelerating rotarod by 6 months of age.

(C) Quantification of expression levels of the soluble fl-mHtt from cortical lysate of two-month-old BACHD, S421D, and S421A mice. Values are based on the mean of three independent blots with mAb 1C2 and compared across different blots by normalization to BACHD samples. Each value was first normalized for input by using the anti-γ-tubulin control. One-way ANOVA analysis reveals that there is a significant difference between the three lines ($F = 22.04$, $p < 0.0001$). Post-hoc Bonferroni analysis indicates that the fl-mHtt expression of the S421A line is significantly different from the BACHD ($p < 0.0001$) and S421D lines ($p < 0.0001$), whereas the BACHD and S421D lines express at similar levels ($p > 0.05$).

****$p < 0.0001$; n.s. not significant.

We next determined if the S421 mutation alters the steady-state levels of soluble fl-mHtt protein during the aging process that could account for an altered phenotype. We used western blots to compare mHtt levels in the cortex of BACHD, S421D, and S421A mice at 1 and 12 months of age. Similar to the BACHD line, S421D or S421A mice showed no significant differences in protein levels with age (Fig. 5a). We then overexposed the blots to look for any obvious changes in the production of soluble mHtt polyQ fragments associated with the S421mutation. We again observed no marked differences at either age (Fig. 5b).

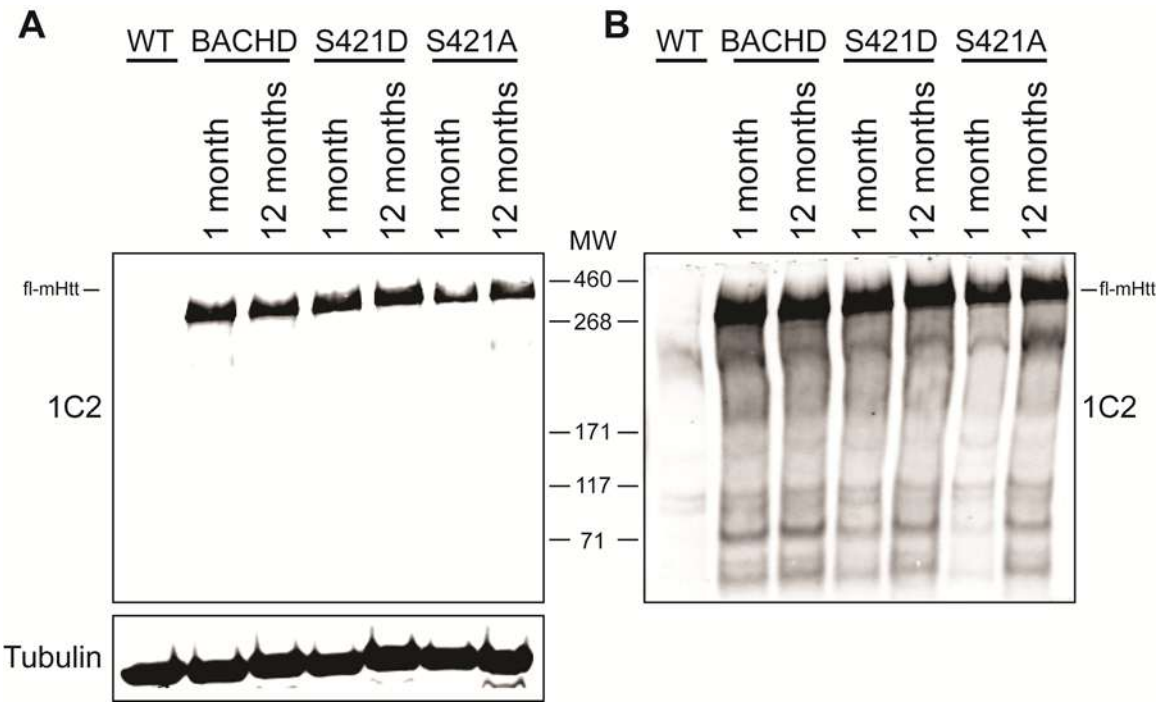

Figure 5. Soluble levels of full-length mutant Huntingtin protein and cleavage into polyQ fragments do not change with age in BACHD, S421D, and S421A mice.

(A) Western blot demonstrates that expression levels of soluble fl-mHtt from cortical lysates of BACHD, S421D, and S421A mice do not change between 1 and 12 months of age. The blot was probed with mAb 1C2 and anti-γ-tubulin as a loading control.

(B) Overexposure of the blot depicted in (A) reveals no marked differences in the production of soluble mHtt polyQ fragments among BACHD, S421D, and S421A mice at either age.

Finally, we sought to confirm that the introduced S421 mutations do not disrupt Htt's essential functions. Complete loss of Htt is embryonic lethal (58), but fl-mHtt can perform the essential functions necessary for murine development and neurogenesis (55, 59, 60) when expressed by its endogenous promoter and regulatory regions. To test whether S421 mutation preserves that ability, we crossed S421D and S421A transgenic mice with mice heterozygous for endogenous Htt for two successive rounds. We genotyped

the progeny at weaning age and found that both the S421D and S421A transgenes were able to rescue embryonic lethality. We confirmed these results by immunoblotting for both transgenic and endogenous Htt in cortical lysates. Mice rescued by transgenic S421D (Fig. 6b) or S421A (Fig. 6c) expressed fl-mHtt but not endogenous murine Htt, as expected. This breeding scheme should produce transgene-positive mice on an Htt null background at an expected Mendelian ratio of one of every seven animals. Consistent with phosphorylation at S421 playing an important role in Htt function, however, S421A-rescued mice were generated at less than the expected ratio (Fig. 6a), suggesting a decrease in fitness during the embryonic or neonatal period. We obtained 10 rescue mice from each of the S421D and S421A lines, and the mice showed no obvious abnormalities through at least 6 months of age.

A

Line	Total Number of Offspring	Expected Number of Rescued Mice	Actual Number of Rescued Mice
S421D	71	10	10
S421A	149	21	10

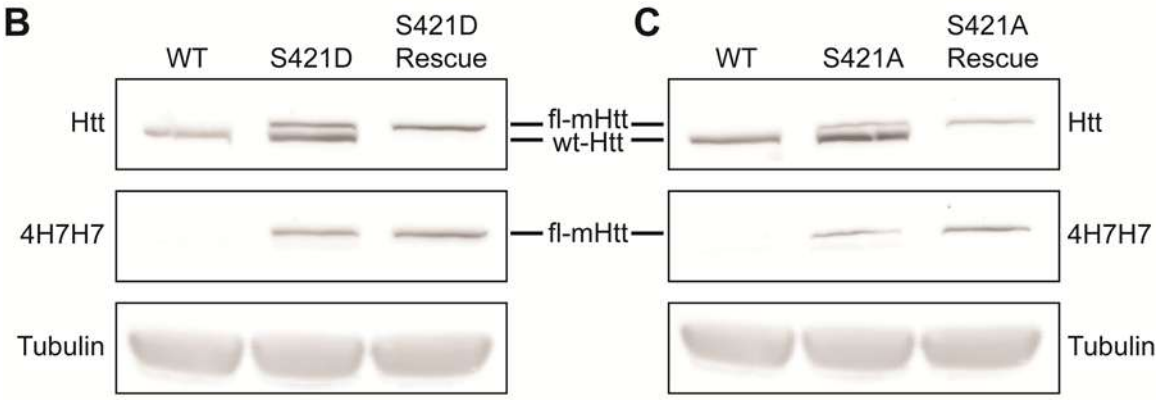

Figure 6. Essential functions of Htt in development can be rescued by expression of transgenic fl-mHtt with phosphomimetic or phosphoresistant mutations at

S421.

(A) Table showing results from two successive rounds of mating between S421D or S421A mice with mice heterozygous for endogenous murine Htt. Complete knockout of endogenous murine Htt is embryonic lethal but can be rescued by transgenic expression of the fl-mHtt BAC construct. The expected ratio of such rescue mice expressing fl-mHtt but not endogenous murine Htt is 1 out of every 7 live mice born, as seen with S421D. S421A lines demonstrate a decreased frequency of rescue.

(B and C) Western blots of cortical lysates probed with anti-Htt (mAb 2166), anti-expanded polyQ (4H7H7), and anti-γ-tubulin confirm that the rescued mice express only fl-mHtt and lack endogenous murine Htt.

Phosphomimetic mutation at S421 strongly ameliorates motor and psychiatric-like deficits caused by the expression of full-length mutant Huntingtin

The neuronal dysfunction elicited by the expression of fl-mHtt in BACHD mice causes early and severe motor phenotypes, with psychiatric-like deficits also emerging at more advanced ages (27, 55, 61). To determine if phosphorylation at S421 affects mHtt-induced neuronal dysfunction *in vivo*, we next sought to determine if the phosphomimetic S421D mutation affects any of these phenotypes. We used a two-way mixed-factorial design to assess repeated performances on the accelerating rotarod at 3, 6, and 12 months of age in a cohort of BACHD, S421D, and WT mice (Fig. 7a). Analysis by two-way repeated measures ANOVA revealed highly significant effects of genotype ($F_{(2,52)}$ = 26.15, $p < 0.0001$) and age ($F_{(2,104)}$ = 4.58, $p = 0.0124$) on the behavioral phenotype. Next, we used Bonferroni post-hoc tests to compare each genotype to each of the others at all ages tested (Table 1). BACHD mice showed a considerably lowered latency before falling off the rotarod when compared to WT littermate controls at all ages tested. On the

other hand, S421D mice were indistinguishable from the WT littermate controls at 3 and 6 months of age, and showed only modest deficits at 12 months of age. At all three ages tested, S421D mice performed substantially better than the BACHD mice. Thus, despite expressing levels of fl-mHtt similar to BACHD mice, S421D animals had a significant mitigation of the accelerating rotarod phenotype.

We considered whether changes in body weight might explain our rotarod results. Weight can influence rotarod performance generally (62), and overexpression of fl-Htt and fl-mHtt in BAC and YAC transgenic mice causes an obesity-with-age phenotype (55, 63). Like the BACHD mice, S421D mice were significantly heavier than WT littermate controls at all three ages tested (Fig. 8). In fact, S421D mice gained weight similar to BACHD mice at 3 and 6 months of age but did not display any deficits at these ages. We therefore conclude that the amelioration of rotarod deficits in S421D mice cannot be explained by differences in body weight.

We next evaluated S421D mice in other motor-dependent behavioral assays at 12 months of age. We used an automated open-field assay to assess general levels of activity and exploratory drive, analyzing the total number of infrared beam breaks over a 10-minute period (Fig. 7b). One-way ANOVA revealed highly significant differences among genotypes ($F_{(2,53)} = 9.031$, $p = 0.0004$). Specifically, BACHD mice were much less active than S421D or WT animals (BACHD versus WT, $p < 0.001$; BACHD vs S421D, $p < 0.05$). In contrast, there were no differences between WT and S421D animals ($p > 0.05$). As a measure of exploratory drive, we also compared the number of hind-limb rearings over the same 10-minute periods (Fig. 7c). Once again, there were significant differences among genotypes (one-way ANOVA: $F_{(2,53)} = 4.910$, $p = 0.0111$). BACHD mice reared fewer times than WT or S421D mice (BACHD versus WT, $p < 0.01$;

BACHD vs S421D, $p < 0.05$), but there were no differences between WT and S421D mice ($p > 0.05$).

As a final measure of motor dysfunction, we analyzed mean hindlimb gait (distance between hind paws) (Fig. 7d). Again, there were considerable differences among genotypes (one-way ANOVA: $F_{(2,45)} = 12.27$, $p < 0.0001$). Consistent with postural instability, BACHD mice maintained a wider base of support than WT and S421D mice (BACHD vs WT, $p < 0.0001$; BACHD vs S421D, $p < 0.01$). Furthermore, no differences were detected between WT and S421D mice ($p > 0.05$). Based on this battery of motor assays, we conclude that S421D animals had either complete rescue or substantial amelioration of motor dysfunction (depending on the assay).

Table 1.

Comparison	3 months	6 months	12 months
S421D vs WT	t = 2.108, p > 0.05	t = 1.767, p > 0.05	t = 3.328 p < 0.01
S421D vs BACHD	t = 3.180, p < 0.05;	t = 3.995, p < 0.001	t = 4.160, p < 0.001
BACHD vs WT	t = 4.933, p < 0.0001	t = 5.561, p < 0.0001	t = 6.865, p < 0.0001

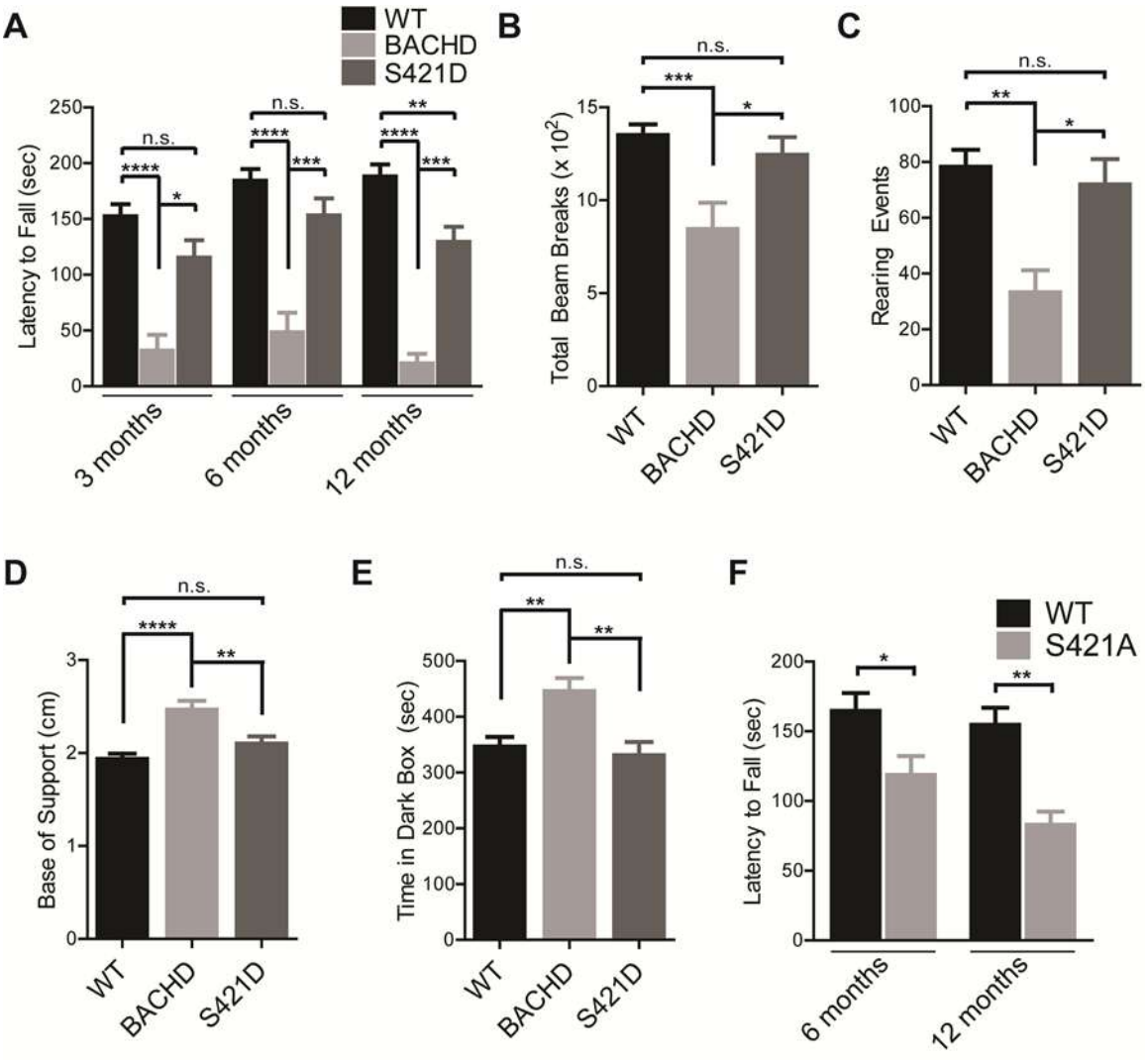

Figure 7. S421D mice but not S421A mice demonstrate ameliorated motor and psychiatric-like behavioral deficits compared to BACHD mice.

(A) A mixed-model two-way repeated measures ANOVA was used to examine performance on the accelerating rotarod of a cohort of BACHD, S421D, and WT mice at 3, 6, and 12 months of age. BACHD mice show significant motor deficits at all ages tested, but S421D mice show no deficits at 3 and 6 months and a significant mitigation of the BACHD phenotype at 12 months.

(B and C) BACHD, S421D, and WT mice were examined in the open field for 10 minutes at 12 months of age and compared by one-way ANOVA. BACHD but not S421D mice demonstrate hypoactivity (B) and decreased exploratory drive (C) compared to WT controls.

(D) Hindlimb gaits of BACHD, S421D, and WT mice at 12 months of age were analyzed with the CatWalk XT (Noldus) and compared by one-way ANOVA. BACHD but not S421D mice have a widened hindlimb gait.

(E) Anxiety-like behavior in BACHD, S421D, and WT mice at 12 months of age was assessed using the light-dark box assay. Over the course of 10 minutes, BACHD but not S421D mice spend more time in the dark box than WT controls.

(F) A separate two-way repeated measures ANOVA was used to examine performance on the accelerating rotarod of a cohort of S421A and WT mice at 6 and 12 months of age. S421A mice perform significantly worse than WT animals at 6 and 12 months of age, consistent with their lower fl-mHtt expression levels.

*$p < 0.05$; **$p < 0.01$; ***$p < 0.001$; ****$p < 0.0001$; n.s. not significant.

BACHD mice demonstrate psychiatric-like deficits at 12 months of age. In particular, they exhibit a higher level of anxiety-like behavior than WT controls in the light-dark box and elevated plus maze (27, 61). We compared the same cohort of mice in the light-dark box to determine if the S421D mutation modifies this phenotype (Fig. 7e). We again found significant differences among genotypes (one-way ANOVA: $F_{(2,43)} = 7.146$, $p = 0.0021$). Consistent with increased levels of anxiety, BACHD mice spent more time inside the dark box than both WT and S421D mice (BACHD versus WT, $p < 0.01$; BACHD vs S421D, $p < 0.01$). S421D mice showed a complete rescue of this phenotype (S421D vs WT, $p > 0.05$). Surprisingly, we did not detect this rescue of phenotype with the elevated plus maze (data not shown).

To control for non-specific effects associated with mutation at S421, we also performed behavioral assays with the S421A animals. Based on their expression levels, these mice would be expected to show modest rotarod deficits beginning at 6 months of age. In agreement with this, we did not detect any differences in these mice at 3 months (data

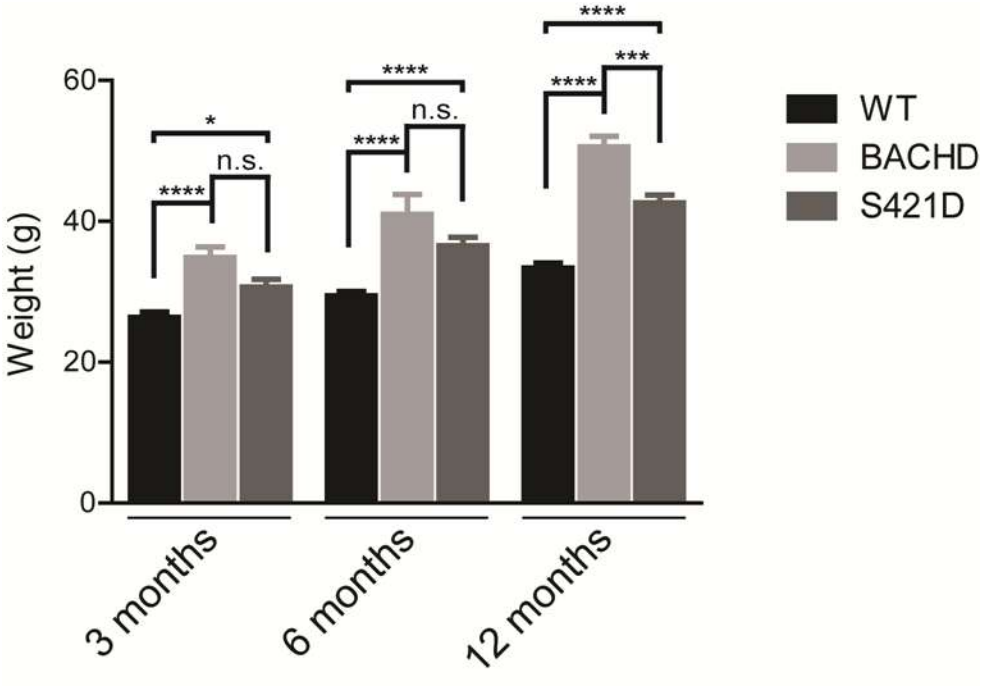

Figure 8. S421D mutant mice display the obesity-with-age phenotype seen in BACHD mice.

Weight measurements of the cohorts of S421D, BACHD, and WT mice prior to the initiation of behavioral testing at each time-point reveals that S421D mutant mice are significantly heavier than WT mice. Data were analyzed by two-way repeated measures ANOVA followed by comparisons of the means with Bonferroni post-hoc tests.

not shown). Significant effects of genotype and age were found by analysis of the data collected at 6 and 12 months of age (Fig. 7f) by two-way repeated measures ANOVA (genotype: $F_{(1,30)} = 11.50$, $p = 0.0020$; age: $F_{(1,30)} = 6.69$, $p = 0.0148$), and we again did

not detect an interaction between the two variables ($F_{(1,30)} = 1.73$, $p = 0.1978$). By post-hoc tests, S421A mice had a lowered latency on the rotarod as compared to WT control mice at both ages (at 6 months: $t = 2.392$, $p < 0.05$; at 12 months: $t = 3.615$ $p < 0.01$).

These behavioral studies demonstrate that phosphomimetic mutation at S421 results in a partial or complete amelioration of both motor and psychiatric-like deficits induced by expression of fl-mHtt. This effect cannot be explained as simply resulting from any mutation at this site unrelated to phosphomimicry, since mice with the S421A mutation to prevent phosphorylation display motor deficits consistent with their significantly lower transgene expression levels.

Phosphomimetic mutation at S421 prevents striatal neurodegeneration caused by the expression of full-length mutant Huntingtin in vivo

Having found that S421D substantially ameliorates both motor and psychiatric-like phenotypes in BACHD mice, we next sought to determine if the phosphomimetic mutation influences neuropathology in BACHD brains at 12 months of age. Specifically, BACHD mice have significant atrophy of the forebrain without accompanying changes in the cerebellum (55), similar to the pattern of degeneration in human HD. To assess this quantitatively, we used unbiased stereology to measure striatal volume in brains from an independent cohort of BACHD, S421D, and WT mice (Fig. 9a, c). There were significant differences among the genotypes (one-way ANOVA: $F_{(2,16)} = 4.665$, $p = 0.0253$). BACHD mice had significantly smaller striatal volumes than WT mice ($t = 2.931$, $p < 0.05$), but S421D mice were similar to the WT controls ($t = 0.7869$, $p > 0.05$).

We also counted striatal NeuN-positive neurons to determine if expression of fl-mHtt caused detectable neuronal loss, taking care to correct our calculations for the changes in volume already measured (Fig. 9b, c). Again, there were significant differences among the genotypes (one-way ANOVA: $F_{(2,16)} = 5.848$, $p = 0.0124$). BACHD mice had fewer striatal neurons than WT mice ($t = 2.719$, $p < 0.05$) and S421D mice ($t = 3.184$, $p < 0.05$), but S421D mice were similar to WT controls ($t = 0.3619$, $p > 0.05$).

We repeated these same studies in the cortex (Fig 9d, e). We observed strong trends among WT, BACHD, and S421D lines similar to those seen in the striatum, in particular for rescue of neuron counts by S421D. However, consistent with cortical degeneration being less profound than striatal degeneration in HD, these trends did not meet statistical significance with this sample size.

These data indicate that expression of fl-mHtt causes atrophy as well as neuronal loss in the striatum, while phosphomimetic mutation at S421 abolishes this neurodegeneration *in vivo*.

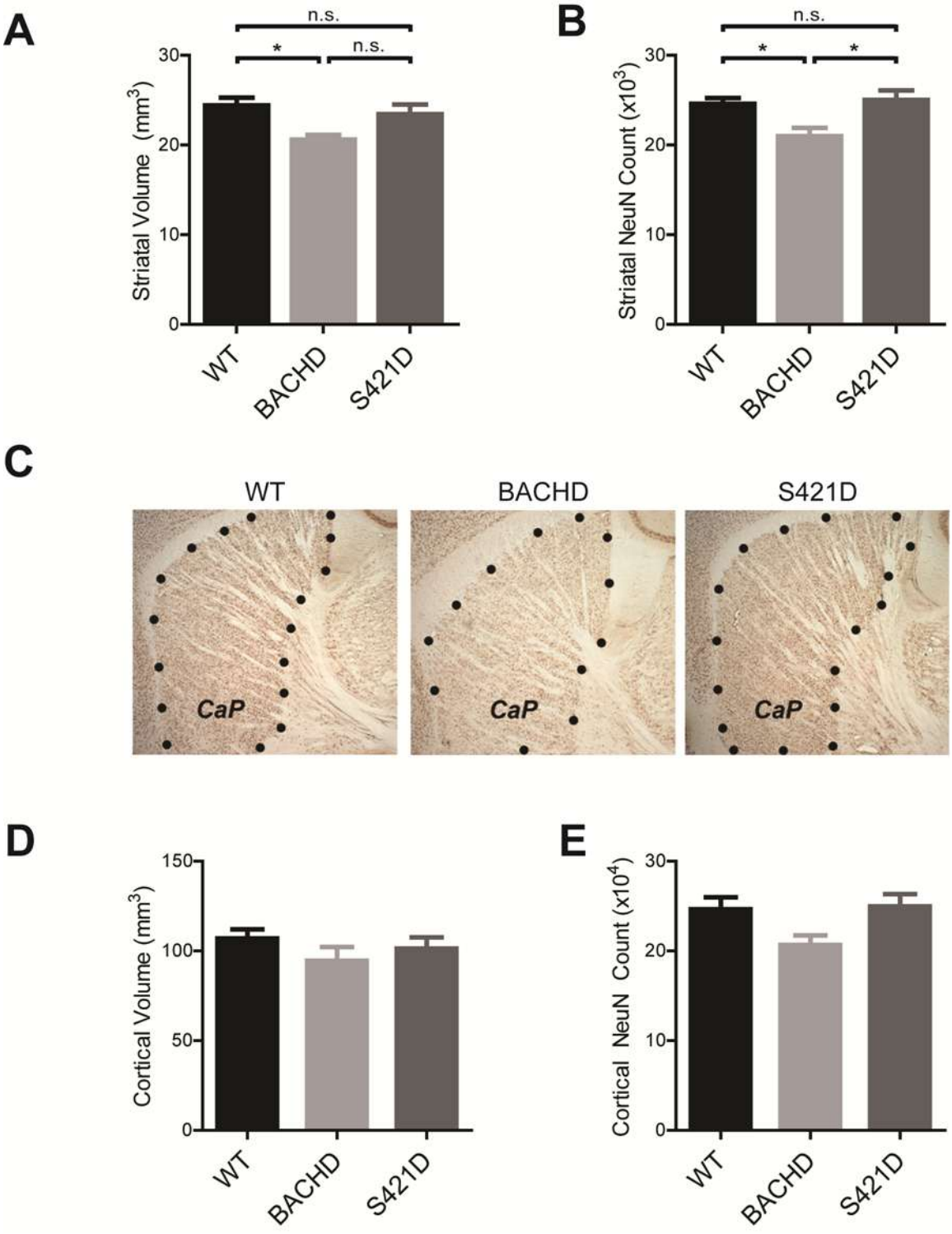
A
n.s.
*
n.s.
Striatal Volume (mm3)
30
20
10
0
WT
BACHD
S421D
B
n.s.
*
*
Striatal NeuN Count (x103)
30
20
10
0
WT
BACHD
S421D
C
WT
BACHD
S421D
CaP
CaP
CaP
D
Cortical Volume (mm3)
150
100
50
0
WT
BACHD
S421D
E
Cortical NeuN Count (x104)
30
20
10
0
WT
BACHD
S421D

Figure 9. S421D rescues the neurodegeneration caused by expression of full-length mutant huntingtin at 12 months of age without substantially altering inclusion body formation.

(A) Measurement of striatal volume by unbiased stereology reveals that BACHD (N = 6) but not S421D (n = 7) mice demonstrate significant striatal atrophy compared to WT (N = 6) controls.

(B) Measurement of striatal NeuN count with correction for volume changes reveals that BACHD mice have significantly fewer neurons than either WT or S421D mice, whereas there is no difference between the WT and S421D mice.

(C) A representative brain slice depicting NeuN staining at low magnification so as to illustrate the striatal boundaries used for stereological measurements.

(D) Measurement of cortical volume by unbiased stereology reveals a trend for cortical atrophy in BACHD mice compared to WT mice.

(E) Measurement of cortical NeuN count reveals a strong trend suggesting that BACHD mice have significantly fewer neurons than either WT or S421D mice, whereas there is no difference between the WT and S421D mice.

*p < 0.05; n.s. not significant.

Phosphomimetic mutation at S421 does not appreciably alter the formation of full-length mutant Huntingtin-induced inclusion bodies in vivo

The formation of inclusion bodies (IBs) by full-length and N-terminal fragments of mHtt is a hallmark of HD pathology. These findings have been recapitulated in mouse models; in fact, the first mouse model of HD led to the initial conclusion that the formation of IBs underlies disease pathology (64). However, later studies (6, 65) contradicted this conclusion and suggested that the formation of IBs is instead a neuronal coping

response. Aged BACHD mice develop IBs that are similar to those observed in the human disease and can be visualized histologically with certain Htt antibodies.

Staining with the polyclonal antibody S830 (66, 67) revealed prominent IBs in both the cortex and striatum of BACHD but not WT mice (Fig. 10), as expected. S421D mice also demonstrated significant levels of IBs that were similar to or perhaps slightly less than those seen in the BACHD animals. This finding is consistent with previous results from primary neurons overexpressing Htt-N480-68Q (31). Thus, despite the substantial amelioration of fl-mHtt-induced behavioral dysfunction and neurodegeneration in S421D mice, widespread formation of IBs still occurs, further supporting the notion that IBs are not in and of themselves the cause of HD.

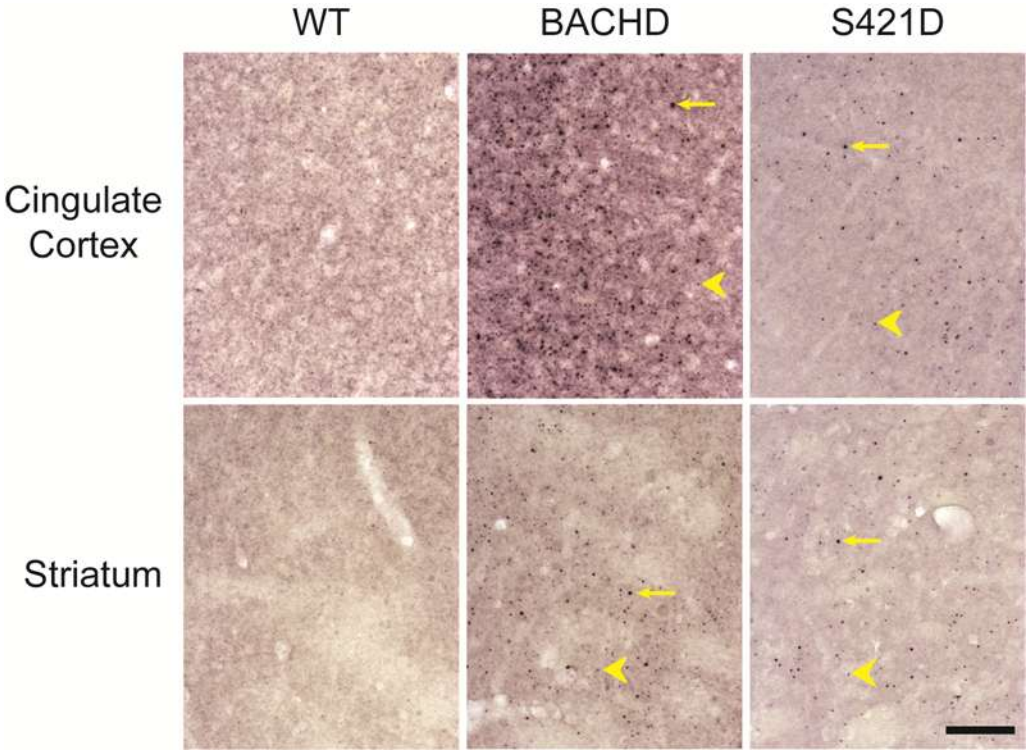

Figure 10. S421D does not substantially alter inclusion body formation.

Immunohistochemistry with monoclonal antibody S830 reveals prominent inclusion bodies in BACHD and S421D striatum and cingulate cortex but not in WT littermate controls. Example smaller (arrows) and larger (arrowheads) inclusion bodies are indicated. The scale bar represents 150 µm, and each field is 600 x 600 µm.

Phosphomimetic mutation at S421 decreases steady-state levels of soluble full-length mutant Huntingtin in the striatum

While analyzing striatal histopathology, we observed that slices from S421D striata were significantly less immunoreactive with mAb 4H7H7 (Fig. 11a, b). This was a surprising finding, as BACHD and S421D express similar levels of fl-mHtt mRNA and protein in the cortex (Fig. 3, 4). A comparison of steady-state levels of soluble fl-mHtt levels in striatal lysates found that S421D mice have a modest but reproducible and statistically significant reduction in soluble fl-mHtt protein compared to BACHD mice ($p = 0.0074$, unpaired t test) (Fig. 11c, d). To determine if the decrease in protein results from a parallel decrease in transcript, we determined striatal mHtt mRNA levels in the lines. As in our previous cortical analyses (Fig. 3e), we found that striatal levels of mHtt mRNA were nearly equivalent in BACHD and S421D mice (Fig. 11e). Thus, changes in expression of the transgene cannot explain the relatively decreased amount of S421D fl-mHtt. Note that these levels of fl-mHtt expression were still higher than those expressed by the S421A mice (Fig. 3b and 3c), implying that a rotarod deficit would be expected by 6 months of age. However, S421D mice had no rotarod deficits at that age (Fig. 7a),

suggesting that lower steady-state striatal levels of soluble fl-mHtt alone do not explain the profound amelioration of the BACHD phenotype in S421D mice.

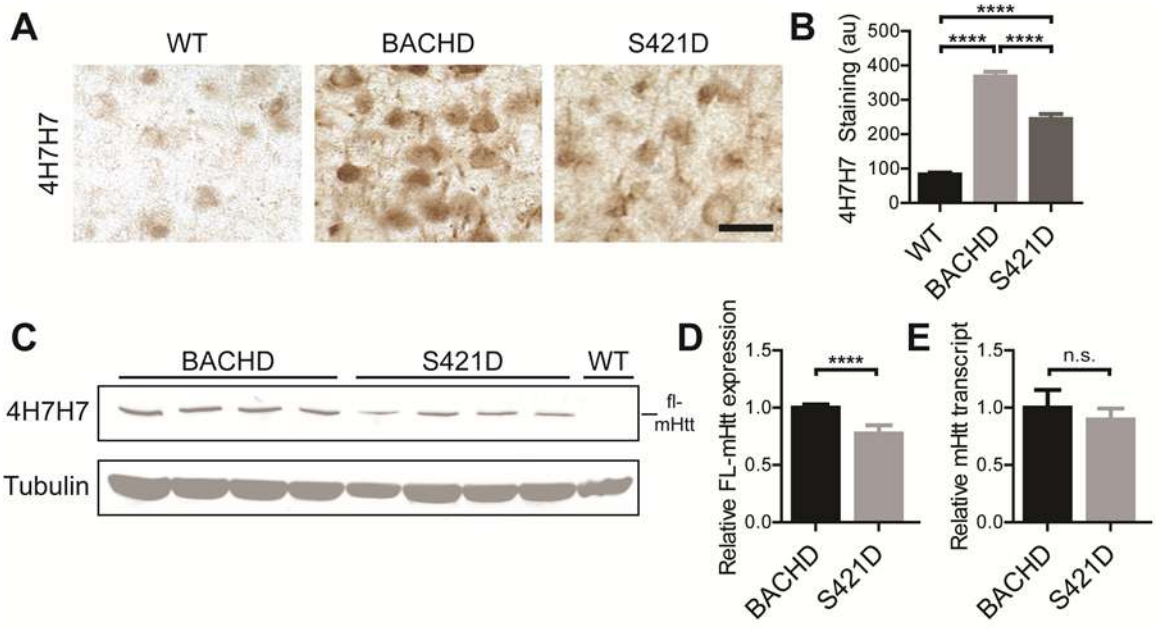

Figure 11. Phosphomimetic mutation at S421 decreases steady-state levels of soluble full-length mutant Huntingtin in the striatum.

(A and B) Immunohistochemistry of striatal sections with anti-polyQ monoclonal antibody 4H7H7 (A) and subsequent quantification of signal intensity (B) suggests that S421D mice express less soluble fl-mHtt in the striatum than BACHD animals, despite expressing similar levels in the cortex (Fig 1). The scale bar represents 20 μm.

(C and D) Western blot with 4H7H7 confirms that S421D mice have less steady-state soluble fl-mHtt than BACHD mice in the striatum. The bar graph displays values based on the mean of three independent 4H7H7 blots of four mice per transgenic line compared across different blots by normalization to BACHD samples. Each value was first normalized for input using the anti-γ-tubulin controls.

(E) S421D mice express levels of mHtt mRNA similar to BACHD animals by reverse-

transcriptase qRT-PCR. The results are from four independent samples per transgenic line, each run in quadruplicate. Values are normalized to BACHD mice and are expressed in arbitrary units (au).

Means were compared with an unpaired t test in D and E. ****p < 0.0001; n.s. not significant.

Phosphomimetic mutation at S421 increases the turnover of an N-terminal fragment of Huntingtin in striatal cells

Having validated S421 as a crucial mediator of fl-mHtt pathology *in vivo* and having found that S421D decreased steady-state striatal levels of fl-mHtt, we returned for further study and validation to the original Htt-N480 constructs that were used to implicate a role for S421-P in mHtt toxicity *in vitro* (31). We reasoned that utilizing ectopic expression would allow us to avoid any possible confounds in the murine system from BAC integration into the host chromatin or from developmental expression of mHtt. Further, it would confirm that any changes in mHtt steady-state levels could be attributed specifically to mutation of S421.

Accordingly, we expressed a myc-actin control and Htt-N480-17Q-S421, -S421D, or -S421A in striatal cell line St14A, as these cells display several properties of striatal MSNs, including expression of the striatal marker DARPP-32 and responsiveness to dopamine receptor agonists (68). Forty-eight hours after transient co-transfection, we lysed the cells. In agreement with our *in vivo* results, phosphomimetic mutation of Htt at S421 decreased steady-state levels of Htt (Fig. 12a, b). Furthermore, cells transfected with the S421A variant of Htt that is incapable of being phosphorylated showed an

increase in steady-state Htt levels over non-mutated Htt-S421 (Fig. 12a, b). These results suggest that phosphorylation of Htt at S421 leads to an increase in its turnover.

We next sought to dissect whether a difference in Htt protein turnover might be attributable to degradation by the proteasome or the lysosome. We treated St14A cells with the specific proteasome inhibitor epoxomicin for 4 hours or with the lysosome inhibitors ammonium chloride and leupeptin for 16 hours and compared Htt accumulation in terms of fold change over control treatment. For all constructs, proteasomal inhibition led to a greater build-up of Htt than inhibition of the lysosome, though the differences did not reach statistical significance. Of note, levels of the S421D construct approximately doubled with proteasome inhibition but were unaffected by lysosome inhibition (Fig. 12c). The combination of decreased Htt-S421D steady-state levels and its accumulation upon epoxomicin treatment imply that phosphomimetic mutation at S421 leads to a significant increase in flux of Htt through the proteasome.

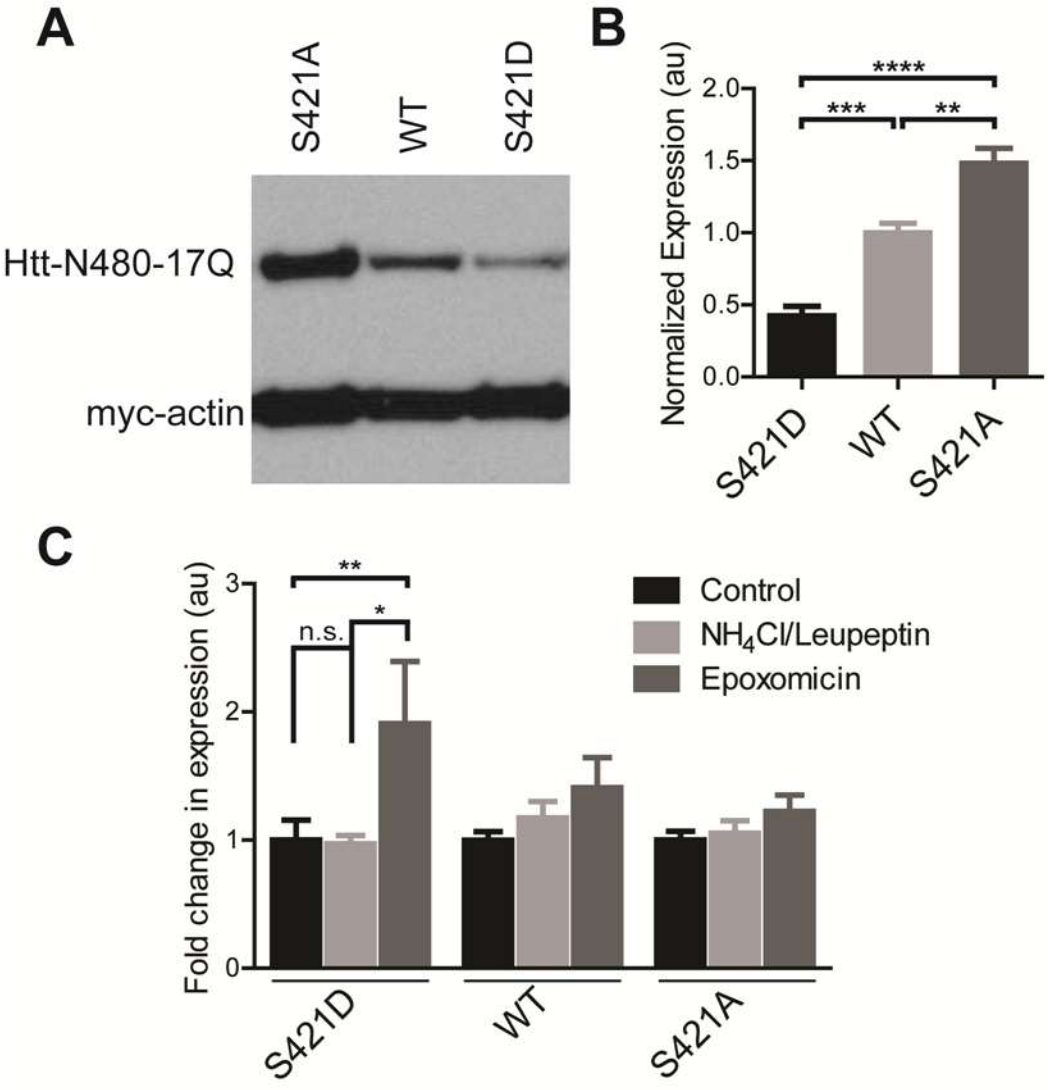

Figure 12. Phosphomimetic mutation at S421 increases the turnover of an N-terminal fragment of Huntingtin in striatal cells.

(A) Representative western blot of St14A cell lysate generated 48 hours after transfection with Htt-N480-17Q and myc-actin. An anti-Htt antibody (mAb 5492) reveals that the S421D mutation decreases steady state levels of Htt relative to WT, whereas the S421A mutation increases it.

(B) Quantification of the effect of S421 mutation on Htt levels in St14A cell lysate. Values are based on the mean of three independent blots after normalization for transfection efficiency and loading with the myc-actin control.

(C) Quantification of the fold change in levels of Htt with and without S421 mutation after treatment with the specific proteasome inhibitor epoxomicin or lysosome inhibitors ammonium chloride and leupeptin suggests that the phosphomimetic S421D mutation increases Htt flux through the proteasome. Values are based on the mean of three independent experiments after normalization for transfection efficiency and loading with the myc-actin control.

*p < 0.05; **p < 0.01; n.s. not significant

Further mechanistic work will be necessary to determine how the S421D mutation ameliorates Htt toxicity. However, both our *in vivo* and *in situ* data imply that S421D causes a decrease in steady-state levels of Htt most prominently in the striatum, and that this change might be caused by increased Htt flux through the proteasome.

Methods

Generation of BAC transgenic mice. Red/ET triple recombination (Gene Bridges GmbH) was used to modify the original BAC vector used to make BACHD mice (55). A 508 bp PCR fragment containing the intended S421A/D point mutation in *HTT* wild type sequences and homology arms to the FRT-PGK- gb2-*neo/km*-FRT selection cassette was generated. BAC-clone RP11-866L6 harbouring *HTT* wild type genomic sequences was used as the PCR-template. The respective point mutations at S421 were inserted by the forward PCR primer (S421D: 5'-GG CAG CTC ACC GCT GCT AAG GAG GAG

TCT GGT GGC CGA AGC CGT AGT GGG GCT ATT GTG GAA CTT ATA GGC AAG TTA-3' ; S421A: 5'-GG CAG CTC ACC GCT GCT AAG GAG GAG TCT GGT GGC CGA AGC CGT AGT GGG GAT ATT GTG GAA CTT ATA GGC AAG TTA-3'). The reverse primer was used to introduce a 70 bp homology arm to the selection cassette (5'-TGC CTT GGG AAA AGC GCC TCC CCT ACC CGG TAG AAT GAA GTT CCT ATA CTT TCT AGA GAA TAG GAA CTT CCT CAA CCT CTT GGG CTT AAG C-3'). During recombination, this homology arm complements a second, independently-amplified PCR-product encoding for the FRT-PGK-gb2-*neo/km*-FRT selection cassette.

Recombineering was then used to assemble both PCR-products and generate BAC-*HTT**S421A/D-FRT-PGK-gb2-*neo/km*-FRT. Expression plasmid pRed/ET encoding for tetracycline resistance (Tc^R) and the Red/ET recombination machinery was electroporated into the BAC. Red/ET-proficient cultures were grown aerobically at 30° C to early exponential phase in the presence of Tc. Expression of the recombination genes was induced by adding 10% (w/v) L-arabinose followed by a temperature shift to 37° C. After one hour of incubation, the cells were washed twice with ice-cold 10% (v/v) glycerol and electroporated with both PCR products. Subsequently, the cells were resuspended in ice-cold LB-medium and grown for 1 h at 1000 rpm and 37° C. Plates supplemented with Chloramphenicol (Cm) and Kanamycin (Km) were used to select for mutants that had undergone successful Red/ET Recombination.

Individual colonies were picked and inoculated the next day. BAC DNA was isolated and analysed by PCR for successful assembling of the construct at the intended position by PCR across the 5' and 3' insertion sites. Clones that displayed the predicted amplicon sizes for the 5´ and 3' insertion were eluted from the gel and subsequently sequenced to confirm proper assembling and integrity. After sequence confirmation, clones were

streaked on plates supplemented with Cm and Km in order to get a pure population of BAC construct *HTT**S421A/D-FRT-PGK-gb2-*neo/km*-FRT.

To remove the selectable marker, plasmid pCi-Flpe was electroporated into the clones with each respective construct. After transformation, 1 ml of LB medium was added to the tube and the cells were incubated for 1.5 hours at 30° C shaking at 700 rpm. The cells were streaked out on LB plates containing Tc, Km, and Cm and incubated for more than 24 hours at 30° C. Colonies were inoculated each in 1 ml of LB medium with Cm, and cells were grown for 3 hours at 30° C. The temperature was subsequently shifted to 37° C, inducing Flpe expression and subsequent FLP recombination of the BAC FRT sites as well as loss of the pCi-Flpe plasmid. Cultures were again streaked out on agar plates containing Cm in order to obtain single colonies. BAC DNA was isolated from the resulting colonies and analysed by PCR to confirm the excision of the selection cassette. The final selected BAC-*HTT**S421A/D-FRT clone was sequenced at regions around the point of mutation, exon1, and the native stop codon to confirm its integrity.

The final modified, sequence-confirmed BACs were prepared as previously described (69) and confirmed to be free of degraded DNA by pulsed-field gel electrophoresis. BAC DNA was linearized overnight with PI-Sce I at 37° C, dialyzed into microinjection buffer, and microinjected into FvB/N pro-nuclei by the Gladstone Transgenic Core.

All mice were maintained in the FvB/NJ background and bred and maintained under standard conditions consistent with National Institutes of Health guidelines and approved by the UCSF Institutional Animal Care and Use Committee.

Genotyping and sequencing. Routine genotyping of BACHD, S421D, and S421A mice was performed by touchdown PCR on tail genomic DNA, amplifying both for mHtt and for an internal control (primer sequences from The Jackson Laboratory) from the mouse genome. The following primers were used: mHtt forward: 5'-CCG CTC AGG TTC TGC TTT TA-3' ; mHtt reverse: 5'-TTG CTG CTG TTG GAA GGA CTT GAG GGA C-3' ; internal control oIMR7338 forward: 5'-CTA GGC CAC AGA ATT GAA AGA TCT-3' ; internal control oIMR7339 reverse: 5'-GTA GGT GGA AAT TCT AGC ATC ATC C-3'.

For sequencing of exon1 (including the CAG-CAA repeat stretch), the region around S421, and the region C-terminal to the native stop codon, tail DNA was purified using the DNeasy Blood and Tissue kit (Qiagen). PCR was performed with the HotStar HiFidelity Polymerase Kit (Qiagen) according to the manufacturer's instructions using the following sets of primers and conditions:

- Exon1_F: 5'-CAG GCT AGG GCT GTC AAT CA-3' ; Exon1-R: 5'-GGT TGC TGG GTC ACT CTG TC-3' ; Annealing temperature 57° C; Q solution included
- S421_F: 5'-CGA GCT TCT GCA AAC CCT GAC-3' ; S421_R: 5'-TTG GCA AGG AAG ATG GAA TGC AG-3' ; Annealing temperature 57° C
- 3'UTR_F: 5'-GCA ACG TGC GTG TCT CTG-3' ; 3'UTR_R: 5'-TGT TCC CAA AGC CTG CTC-3' ; Annealing temperature 55° C

The PCR product was purified using the DNA Clean & Concentrator kit (Zymo Research Corp.) and submitted for sequencing (Elim Biopharmaceuticals, Inc.).

Preparation of brain lysates and western blotting. Mouse brains were dissected on ice, snap frozen on dry ice, and stored at -80° C until further use. Brains were homogenized in a modified RIPA buffer (55), supplemented with Halt Protease and

Phosphatase Inhibitor Cocktails (Thermo Sci), using a pellet pestle (Kontes). The samples were then centrifuged at 4° C for 15 min at 13,000 rpm. The soluble supernatant was retained, and protein concentration was determined using the BCA Protein Assay (Thermo Sci).

For Western blots, we used the NuPAGE (Invitrogen) 3-8% Tris-Acetate or 4-12% Bis-Tris pre-cast gels. Samples (40µg) were prepared with NuPAGE LDS buffer and reducing agent and heated for 10 min at 70° C according to the manufacturer's instructions. After resolution by PAGE, protein was wet-transferred onto Immobilon-FL (Millipore) polyvinylidene difluoride (PVDF) using NuPAGE transfer buffer with no added methanol. Immunoblots were probed with 4H7H7 (1:5000), 1C2, (Millipore, MAB1574, 1:3000), anti-Htt 2166 (Millipore, mAb2166, 1:3000), anti-γ-tubulin (Sigma, T6557, 1:20,000), or our affinity-purified rabbit phosphospecific anti-S421-P (1:200) (see subsequent methods). Appropriate IRDye secondary antibodies (LI-COR Biosci) were used at a 1:20,000 dilution unless otherwise noted. Images were captured with the Odyssey CLx (LI-COR Biosci). To visualize anti-S421-P blots of brain lysate, a polyclonal goat anti-rabbit HRP conjugated secondary antibody (Dako) detected with SuperSignal West Femto chemiluminescent substrate (Thermo Sci) was utilized.

Preparation of RNA extracts and qRT-PCR. Mice were maintained undisturbed in their home cage until immediately prior to extraction. They were subsequently anesthetized to a surgical plane of anaesthesia with isoflurane and decapitated with a sharp pair of scissors. Brains were then removed, dissected on ice, snap frozen with liquid nitrogen, and stored at -80° C until further processing. RNA was isolated and purified with the

miRNeasy Mini kit (Qiagen) according to the manufacturer's instructions, with frozen tissue being disrupted and homogenized with the TissueLyser II (Qiagen).

20ng of RNA was converted to cDNA using the Taqman Reverse Transcription kit (Invitrogen) using a 1:1 mix of random hexamers and oligo dT. qRT-PCR with Sybr Green (Applied Biosystems) was performed on 1:40 dilutions of the samples using a 7900HT Fast Real-Time PCR system (Applied Biosystems). We generated primers that anneal specifically to human Huntingtin mRNA (QuantPrimer; Arvidsson et al 2008):
Htt_F: 5'-ATC CCG GTC ATC AGC GAC TAT C-3' ; Htt_R: 5'-GCT TGT AAT GTT CAC GCA GTG G-3'
Samples were normalized using primers for mouse beta actin (QuantiTect primers, Qiagen). The standard curve method was used to analyse the data.

Genetic rescue of embryonic lethality of complete loss of endogenous huntingtin. The genetic rescue of murine Htt knockout embryonic lethality was performed as previously described (55). Briefly, hemizygous BACHD-S421D and BACHD-S421A animals were bred with murine *Hdh* heterozygous mice (58). Mice identified as transgene positive and *Hdh* heterozygous by PCR analysis of tail DNA were then bred for another round with the *Hdh* heterozygous mice. Progeny of this cross were weaned at 3 weeks and genotyped. Rescue mice were defined as mice without either of the two endogenous *Hdh* alleles but with the hemizygous S421D or S421A BAC transgene. As previously reported (58), no mice were born completely null for the *Hdh* alleles unless the transgene was also present.

Behavioral testing. All testing was performed during the light phase of the light cycle, and animals were given at least 45 minutes to acclimate to the testing room.

Approximately equal numbers of males and females were used per each genotype. Data was collected blind to genotype. All apparatuses were cleaned with 70% ethanol between each run.

Accelerating rotarod. Motor performance was examined on the accelerating rotarod in a cohort of BACHD (N = 7), S421D (N = 17), and WT (N = 31) mice at 3, 6, and 12 months of age and a cohort of S421A (N = 13) and WT (N = 19) mice at 6 and 12 months of age. Only mice with data collected at each time point were analyzed. Before each time point, mice were trained on the rotarod at 16 rpm for three trials. The subsequent two days, mice were tested twice a day, three times each session, as it accelerated from 4 to 40 rpm over 5 minutes.

Open field. Total activity and rearing activity was assessed in an automated clear plastic chamber (41 x 41 x 30 cm) Flex-Field/Open-Field Photobeam Activity System (San Diego Instruments). Mice were placed in open-field chambers with two 16 × 16 photobeam arrays to detect horizontal and vertical movements. Total beam breaks and number of rears (the number of times the mouse stood erect on its hindlegs) were measured automatically by the instrument over 10 minutes.

Gait assessment. The CatWalk XT (Noldus) was used to automatically assess the mean hindlimb gait. Mice were placed on the apparatus and were removed after three runs that were judged compliant by the software (version 9.1) with its default settings. Paw identification was performed automatically by the software with human review of each call to confirm accuracy.

Light-dark box. Anxiety-like behavior was assessed in a light-dark box created with the open field chamber described previously with the dark box insert (San Diego Instruments catalog #7001-0364) added. This insert encloses half of the chamber in darkness with a small opening allowing free passage of the mouse between the light and dark sides. The amount of time spent in each chamber by a mouse during the ten minute test was measured automatically by the instrument. The test was conducted under standard lighting conditions.

Stereology and Immunohistochemistry. Avertin was used to bring mice to a surgical plane of anesthesia, as confirmed by paw pinch and the corneal reflex. A thoracotomy was performed and the right atrium was ruptured with a forceps. An automated pump was used to perfuse saline into the left ventricle via butterfly needle, and the pump was run until completion of the perfusion as judged by the lack of further blood draining from the right atrium as well as blanching of the liver. After decapitation, brains were removed from the skull and the left hemisphere was further dissected on ice as needed for biochemistry. The right hemibrain was immersion-fixed in 4% paraformaldehyde in PBS at 4° for 48 hours. The volume of the neocortex was estimated in sagital brain sections sectioned with the vibratome at 50 µm. Sections were immunostained with anti-NeuN or mAb 4H7H7, washed with PBS, incubated in biotinylated secondary antibody followed by avidin coupled to horseradish peroxidase, placed in 20% diaminobenzidene (DAB), mounted, dried, and coverslipped with Entillin. Sections were analyzed at 63X using a digital Olympus BX51 microsocope and a Stereo Investigator system (MBF Biosciences, Williston, VT). Neocortex was divided into regions according to the criteria of the Allen Brain Atlas (mouse.brain-map.org), which includes insular, temporal, cingulated, motor, orbital, parietal, prelimbic, perirhinal, retrosplenial, somatosensory and visual cortices. Volume was estimated by point counting using Cavalieri's method. Grid spacing for

coronal sections was 600 μm and 300 μm respectively. For each brain every tenth section was analyzed. Volume was estimated for the right hemisphere and multiplied by 2 to estimate total neocortical volume. Neocortical volume was blindly re-measured on a subset of sections to assess intra-observer reliability. For neuron counts, the total number of positive cells was averaged and expressed as relative numbers per area after accounting for any changes in volume.

Immunohistochemical staining of mutant Huntingtin inclusion bodies. Multiple perfusion-fixed brains were embedded in gelatin blocks, post-fixed, and freeze-cut into coronal 35μm sections in 24 sequential series (NeuroScience Associates, Inc., Knoxville, TN). These were stored at -20° C in cryoprotectant as individual series of sections and stained for mutant Htt-derived aggregates with an affinity purified preparation of the sheep anti-Htt antibody S830 (30 ng/mL) under uniform free-floating conditions modified from previous descriptions (70). Binding was visualized using ultra-sensitive HRP-based Ni++/DAB immunohistochemistry. Images were collected on a Spot Slider camera on a Leica DMR microscope under the control of Image Pro Plus (Media Cybernetics, Rockville, MD), and minimal manipulations of images was performed in Adobe Photoshop CS12.0. Each field is 600 x 600 microns.

Generation of S421-P phosphospecific antibodies. Affinity-purified antibodies were generated from rabbit serum as previously described (31) using the following phosphopeptide as immunogen: CSGGRSRSGpSIVELI. To increase sensitivity and specificity, subsequent boosts were performed with a shortened version of the peptide: CGRSRSG(pS)IVEL. For purification of the serum, a negative depletion technique was used to enrich for phosphospecific antibody by running the crude serum over a column

of the phosphorylated peptide. Bound antibodies were then eluted and depleted by running over a column with the non-phosphorylated peptide.

Analysis of Huntingtin steady-state levels and clearance. N480-17Q Htt constructs with or without mutation at S421 (31, 43) were cotransfected with Lipofectamine 2000 (Invitrogen) into St14A cells along with myc-actin to control for transfection efficiency. When indicated, cells were treated for 4 hours with DMSO or 100 nM epoxomicin in DMSO or for 16 hours with water or 20 nM ammonium chloride/100 μM leupeptin in water. The short incubation time for epoxomicin treatment was used to eliminate the possibility of non-specific effects of epoxomicin on the lysosome. Cell culture, lysis, and Western analysis were performed as previously described (28) with slight modifications as follows. NuPAGE Novex 4-12% Bis-Tris pre-cast gels with MOPS running buffer (Invitrogen) were used with 20 μg of sonicated whole cell lysate. Quantitative densiometric analysis was performed on digitalized images of immunoblots using ImageJ (NIH). Water and DMSO control condition measurements were found to have no statistically significant differences and were combined for the remainder of the statistical analyses.

Statistical analyses. All data are shown as the mean ± standard error of the mean (SEM) unless otherwise noted. For all statistical analysis, Prism 5 software (GraphPad, San Diego, CA) was used with a significance level set at 0.05. For group comparisons, one- or two-way ANOVAs were performed as indicated with Bonferroni post hoc analysis for pairwise comparisons unless otherwise stated. When appropriate, means of two groups were compared with an unpaired two-way t test.

Chapter 3: BDNF transcriptional dysfunction is minimal in BACHD mice

Introduction

As discussed previously, BDNF is a crucial extracellular trophic factor and signaling molecule implicated in core brain processes and neuronal survival (12). Furthermore, the striatum produces little of its own BDNF and instead crucially depends on its delivery from other brain regions, particularly the cortex (13-15). Several studies have implicated a mHtt-mediated reduction of BDNF at the transcriptional level as an important contributor to HD pathogenesis (17-19), and increasing forebrain BDNF levels via transgenic overexpression or reducing BDNF levels via partial knockout improved or worsened phenotypes in mouse models of HD, respectively (71-74). Apparently, WT but not mHtt facilitates *BDNF* transcription (16) due to the presence of an RE1/NRSE (repressor element 1/neuron-restrictive silencer element; referred to herein as RE1) locus in the *BDNF* exon II promoter, where REST/NRSF (RE1 silencing transcription factor/neuron-restrictive silencing factor; referred to herein as REST) can bind and inhibit transcription (75). WT Htt binds REST and keeps it sequestered in the cytosol, thereby preventing BDNF gene silencing. However, mHtt has a decreased affinity for REST, allowing it to enter the nucleus and repress transcription. Bioinformatics suggest that RE1 sites are found in a large number of neuronal genes (76), implying that Htt could be involved in regulating many other genes. Similarly, many RE1 sites are found in genes important for neuronal function, including synaptic transmission, and many of these target genes are dysregulated either in HD patients or in mouse models of HD, including *BDNF* (77). Consistent with this previous work, upon initial characterization BACHD

brains were reported to show a significant (~50%) deficit in cortical *BDNF* transcription at 6 months of age (55).

Additional molecular details have been reported on the REST-Htt interaction. It involves an indirect association via a complex of Htt, HAP1, and $p150^{Glued}$ (a subunit of the dynactin complex), which together interact with RILP (REST/NRSF-interacting LIM domain protein), which in turn binds to REST (78). The complex of Htt, HAP1, and $p150^{Glued}$ previously has been studied in the context of the role Htt plays in axonal trafficking. Gauthier and colleagues (79) found that this complex binds dynein and kinesin motors to facilitate the anterograde and retrograde axonal trafficking of vesicles, which in turn interact with the molecular motors via other components of the dynactin complex. PolyQ expansion of Htt, however, abrogated the stimulation of vesicular trafficking. Biochemical studies revealed an increased interaction between HAP1 and mHtt, in turn correlating with a decrease in the association between the molecular motors and the microtubules (Fig. 13a). Later work from the same laboratory reported that phosphorylation of mHtt at S421 restored its function in axonal transport and restored the normal interaction between Htt and HAP1 (45).

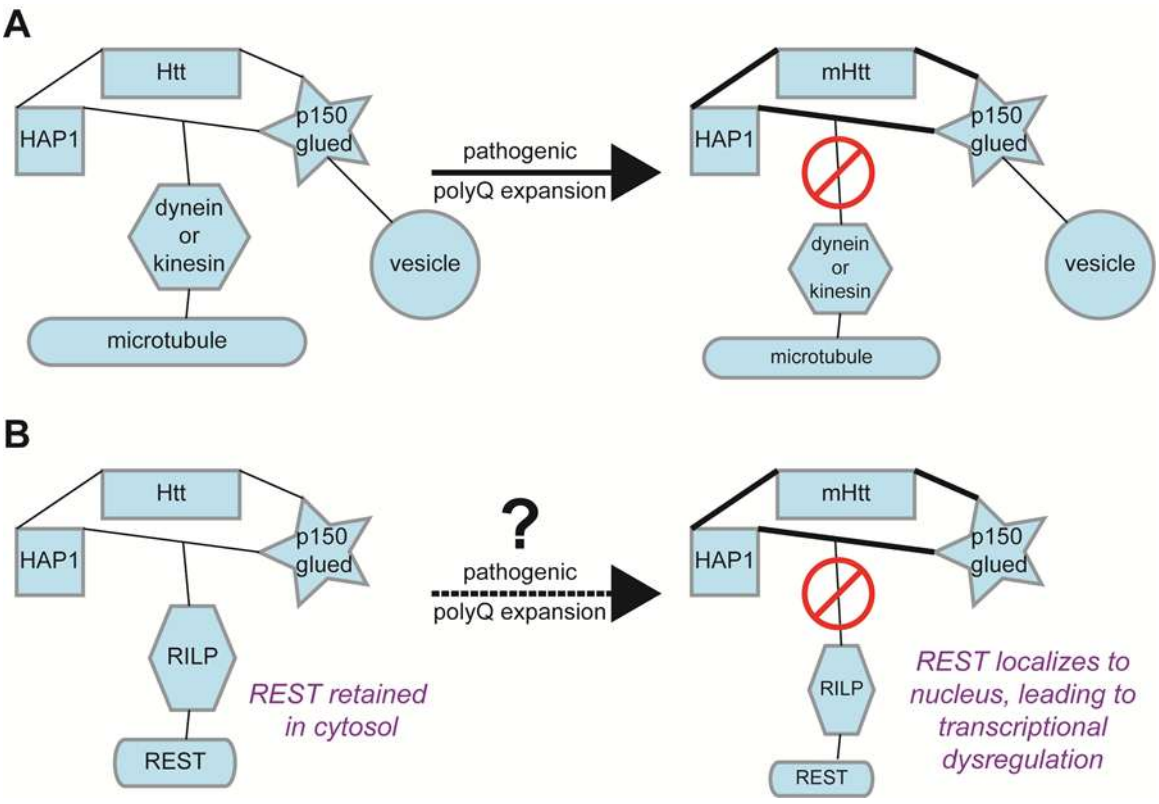

Figure 13. Cartoon schematic of the relevant Htt-HAP1-p150Glued complexes and their putative dysfunction in HD.

(A) The complex has been shown to associate with microtubules and molecular motors to facilitate vesicular trafficking (left). However, mHtt binds to the complex more tightly (bolded lines), thereby decreasing the association with molecular motors and leading to a reduction in vesicle movement (right).

(B) The same complex has been reported to bind REST indirectly via RILP in order to sequester REST in the cytosol and prevent it from acting on RE1 sites in the nucleus (left). We hypothesized that mHtt might cause an analogous decrease in association of the complex with RILP, thereby allowing REST to localize to the nucleus and alter transcription (right).

Given the apparent biochemical similarities between the interactions of the Htt, HAP1, and p150^{Glued} complex with molecular motors and RILP-REST, we hypothesized that S421-P might ameliorate mHtt-mediated *BDNF* transcriptional dysfunction specifically and the associated anticipated REST/NRSE dysregulation more generally in BACHD mice (Fig. 13b). As we investigated this possibility, however, we found no evidence of significant transcriptional dysfunction for *BDNF* or *Synapsin I (Syn-1)*, another REST-regulated gene. Thus, we conclude that *BDNF* transcriptional dysfunction and the Htt-REST interaction are responsible for little if any of the mHtt-evoked phenotype observed in BACHD mice.

Results

We first attempted to recapitulate the reported *BDNF* transcriptional decrease in the cortex of BAHCD mice at 6 months of age (55). We isolated RNA from BACHD mice and WT littermate controls and converted it to cDNA. We then performed qRT-PCR using the same two sets of primers to amplify *BDNF* cDNA as had been used previously. These primers, which amplify both the coding region and exon IV of *BDNF* cDNA, respectively, demonstrated at least a 50% reduction in *BDNF* transcription in the previous report (55). To our surprise, however, we detected no significant decrease with either set of primers (Fig. 14a, b). To follow up on this finding, we sought another neuronal gene known to be regulated by REST to look for any evidence of the widespread REST-mediated transcriptional dysfunction that has been reported in HD (77). *Syn-1* is such a gene (80). Just as for *BDNF*, we did not detect any changes in *Syn-1* transcription (Fig. 14c).

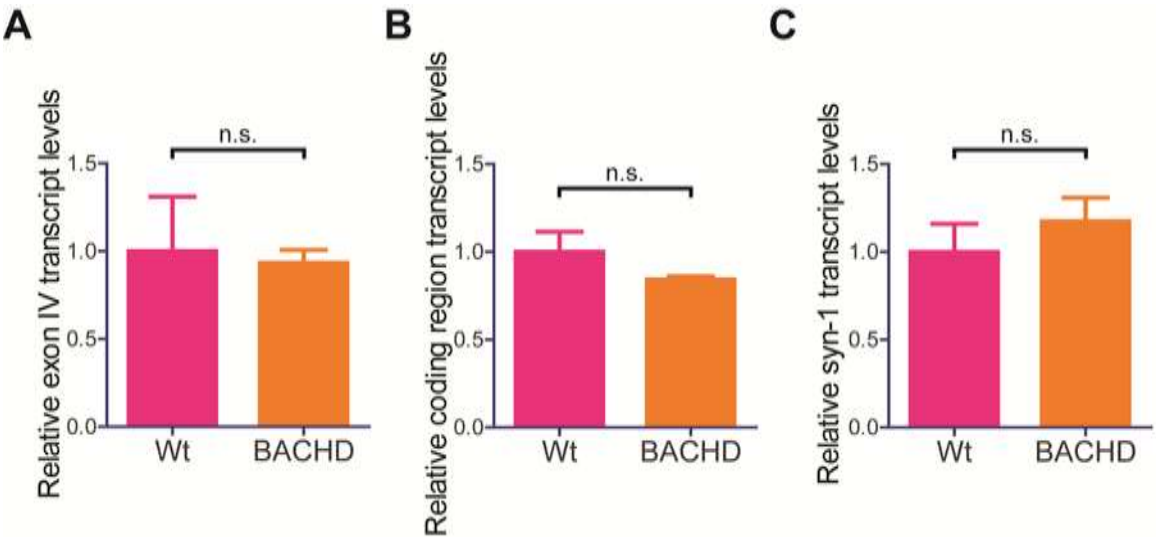

Figure 14. qRT-PCR of BACHD cortex detects no changes in BDNF or Syn-1 transcription.

qRT-PCR on cDNA generated from BACHD and WT littermate controls at 6 months-of-age revealed no statistically significant differences in *BDNF* transcription utilizing previously published primers that amplify exon IV (A) or the coding region of *BDNF* (B), respectively. (C) No differences were found in transcript levels of *Syn-1*, a gene strongly regulated by REST.

Error bars indicate mean ± SEM; n.s., not significant by unpaired t test.

Given the unexpected nature of these findings and the limitations of any single negative result, we sought to confirm our data with other experimental approaches that have non-overlapping caveats and limitations. To address the concern of significant RNA degradation during the harvesting of brain tissue, we bred a new cohort of BACHD mice and WT controls. At 8 months of age, we isolated cortex, striatum, and cerebellum of these mice, and to minimize any RNA degradation the mice were rapidly anesthetized and decapitated, brains were dissected on ice, and tubes were snap-frozen in liquid nitrogen. To minimize any transcriptional changes that might be evoked by the process of removing mice from their holding room and bringing them into the necropsy room,

only one cage (≤ 5 mice) was brought to the room at a time and the cages were not disturbed in any way until that moment. After completion, we again isolated RNA and created the associated cDNA. In collaboration with the Institute for Systems Biology, we performed whole transcriptome shotgun sequencing (RNA-seq) to look for global transcriptional changes in BACHD mice (H.Z., I.K., S.F., unpublished data). In agreement with our original qRT-PCR data, there were no significant changes in *BDNF* or *Syn-1* in any of the three brain regions analyzed (data not shown).

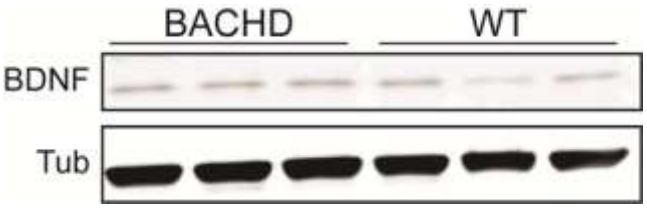

Figure 15. No significant changes in BDNF protein in BACHD mice.

Western blot of soluble cortical lysate of 12-month-old BACHD and WT littermate controls reveals no significant differences in BDNF at the protein level. γ-tubulin was used as a loading control.

As a final approach, we looked at BDNF protein itself in the cortex of 12-month-old BACHD and WT littermate control mice. Western blots of soluble cortical lysate detected no changes in BDNF (Fig. 15). We also employed immunohistochemistry to stain for BDNF (A.O., I.K., S.F., unpublished data). While BDNF was clearly decreased in the R6/2 mouse model of HD based on overexpression of an exon1 fragment of mHtt, there was no decrease in BDNF in BACHD retrosplenial cortex, as consistent with our prior results. In fact, BDNF levels actually were higher in this brain region in BACHD mice compared to WT controls (data not shown). This finding could be consistent with BDNF accumulation caused by mHtt-induced deficits in its anterograde trafficking. In sum, these results further support our

findings that BDNF transcriptional dysfunction and the Htt-REST interaction are not required for the mHtt-evoked phenotype observed in BACHD mice.

Methods

RNA collection and cDNA creation for qRT-PCR

Avertin was used to bring mice to a surgical plane of anesthesia, as confirmed by paw pinch and the corneal reflex. A thoracotomy was performed and the right atrium was ruptured with a forceps. An automated pump was used to perfuse saline into the left ventricle via butterfly needle, and the pump was run until completion of the perfusion as judged by the lack of further blood draining from the right atrium as well as blanching of the liver. After decapitation, brains were removed from the skull, snap frozen on dry ice, and stored at -80° C until further processing. RNA was isolated and purified with the RNeasy Lipid Tissue Mini kit (Qiagen) according to the manufacturer's instructions, with frozen tissue being disrupted and homogenized initially by pipetting and finally with the QIAshredder (Qiagen). 300 ng of RNA was converted to cDNA in a 50 µl reaction using the Taqman Reverse Transcription kit (Invitrogen) using a 1:1 mix of random hexamers and oligo dT's.

qRT-PCR

qRT-PCR with Sybr Green (Applied Biosystems) was performed on 1 µl of the aforementioned cDNA using a 7900HT Fast Real-Time PCR system (Applied Biosystems). Primers used for mouse *BDNF* (55), *syn-1*, and *β-tubulin* were as follows: *BDNF* exon IV, forward: 5'-GCA GCT GCC TTG ATG TTT AC-3' ; *BDNF* exon IV, reverse: 5'-CCG TGG ACG TTT ACT TCT TTC-3'; *BDNF* coding sequence, forward: 5'-

ATT AGC GAG TGG GTC ACA GC-3'; *BDNF* coding sequence, reverse: 5'-TCA GTT GGC CTT TGG ATA CC-3'; *Syn-1*, forward: 5'-AGC TCA ACA AAT CCC AGT CTC T-3' ; *Syn-1*, reverse: 5'-CGG ATG GTC TCA GCT TTC AC-3' ; *β-tubulin*, forward: 5'-GAT CGG TGC TAA GTT CTG GGA-3'; *β-tubulin*, reverse: 5'-AGG GAC ATA CTT GCC ACC TGT.

Samples were analysed using the delta-delta Ct method with *β-tubulin* used for normalization.

RNA collection and cDNA creation for RNAseq

Mice were maintained undisturbed in their home cage until immediately prior to extraction. They were subsequently anesthetized to a surgical plane of anaesthesia with isoflurane and decapitated with a sharp pair of scissors. Brains were then removed, dissected on ice, snap frozen with liquid nitrogen, and stored at -80° C until further processing. RNA was isolated and purified with the miRNeasy Mini kit (Qiagen) according to the manufacturer's instructions, with frozen tissue being disrupted and homogenized with the TissueLyser II (Qiagen). 20 ng of RNA was converted to cDNA using the Taqman Reverse Transcription kit (Invitrogen) using a 1:1 mix of random hexamers and oligo dT's.

Preparation of brain lysate and western blotting

Mice were anesthetized to a surgical plane of anaesthesia with isoflurane and decapitated with a sharp pair of scissors. Mouse brains were removed, dissected on ice, snap frozen on dry ice, and stored at -80° C until further use. Brains were homogenized in a modified RIPA buffer (55) supplemented with Halt Protease and Phosphatase Inhibitor Cocktails (Thermo Sci) using a pellet pestle (Kontes). The samples were then

centrifuged at 4° C for 15 min at 13,000 rpm. The soluble supernatant was retained, and protein concentration was determined using the BCA Protein Assay (Thermo Sci).

For Western blots, we used Mini-PROTEAN TGX 12% pre-cast gels (BioRad). Samples (70 µg) were prepared with standard Laemmli sample buffer supplemented with 2-mercaptoethanol as the reducing agent and boiled for 5 min. After resolution by PAGE using tris-glycine SDS running buffer, protein was wet-transferred onto Immobilon-FL (Millipore) polyvinylidene difluoride (PVDF) using tris-glycine transfer buffer with 20% methanol overnight at 25 V constant at 4° C. Immunoblots were probed with anti-BDNF (abcam, ab6201, 1:500) and anti-γ-tubulin (Sigma, T6557, 1:20,000). Appropriate IRDye secondary antibodies (LI-COR Biosci) were used at a 1:20,000 dilution. Images were captured with the Odyssey CLx (LI-COR Biosci).

Chapter 4: Discussion

In this work, we show that phosphomimetic mutation at S421 strongly ameliorates the toxicity of fl-mHtt *in vivo* and that significant dysregulation of BDNF or REST-mediated transcription does not appear to be required to evoke the BACHD phenotype. We found that the S421D mutation prevented the onset of a variety of behavioral phenotypes and the selective striatal neurodegeneration that occurred in unmodified BACHD mice. Conversely, the S421A mutation did not prevent the development of a behavioral phenotype proportional to mHtt expression levels. Thorough characterization of the S421D mutant mice revealed that the phosphomimetic mutation did not alter the ability of the mHtt transgene to rescue the embryonic lethality of Htt knockout, and it mitigated behavioral and histopathological phenotypes without significantly altering IB formation. Surprisingly, while S421D mice had similar levels as BACHD mice of both Htt mRNA and soluble protein in the cortex, they had relatively decreased steady-state levels of protein but not mRNA in the striatum. Furthermore, biochemical analyses confirmed that the S421D mutation decreased the steady-state levels of soluble Htt in a striatal cell line and suggested that this occurs via increased Htt flux through the proteasome. In sum, these results specifically validate S421-P as a therapeutic target in HD and further support strategies aimed at increasing mHtt turnover in the striatum as a promising treatment approach.

The significant impact of phosphomimetic mutation of S421 on mHtt toxicity reported here extends previous studies (31, 42, 44, 48) to a transgenic mouse model of HD that expresses fl-mHtt under the control of its endogenous promoter and regulatory regions. Comparing a line of S421D mice with expression levels similar to the unmodified

BACHD mice was of critical importance, both in terms of meaningful interpretation of altered behavioral and histopathological phenotypes and for detecting changes in protein turnover. That S421D has such a drastic effect on the disease phenotype underscores the critical role that protein context plays in polyQ-mediated toxicity (22, 23) and confirms that PTMs seemingly more distant from the disease-associated mutation nevertheless can still modify disease pathogenesis in a crucial manner (24, 81).

Our study also determined that preventing phosphorylation at S421 did not significantly increase fl-mHtt toxicity, as might have been expected. However, disease-associated expansion of the polyQ repeat was shown previously to significantly decrease the amount of Htt phosphorylated at S421 in both cells and mouse brains (44, 50). The low levels of mHtt phosphorylation we detected in BACHD cortex agree with these prior findings and might explain why S421A mice did not show a more aggressive phenotype. In the setting of low baseline levels of phosphorylation, S421A is expected to be the more conservative mutation. On the other hand, the permanent addition of a negative charge via aspartic acid mutation to mimic tonic phosphorylation represents a more drastic change. In agreement, not only did the S421D mice demonstrate remarkable amelioration of the HD phenotype, but the striatum showed a complete rescue of neurodegeneration. In a striatal cell line expressing Htt-N480-17Q, however, the S421A mutation did have a significant effect diametrically opposite to that of S421D. The higher S421-P levels in the context of this non-pathogenic Htt fragment presumably allowed for the effects of the S421A mutation to become more apparent.

This work also revealed that the S421D mutation led to a decrease in striatal steady-state fl-mHtt levels, suggesting increased mHtt flux through the proteasome. Whereas phosphomimetic mutation of serines 13 and 16 drastically alters Htt's aggregation

properties (27), S421D did not appreciably alter IB formation, suggesting that misfolded polyQ stretches are still present and being recognized by neurons. If true, this would imply that S421D-mediated amelioration of mHtt toxicity occurs at least in part via other mechanisms. Htt previously has been connected to protein-turnover pathways (82, 83), and increasing reports of phosphorylation-dependent ubiquitination in other proteins (84) offers one plausible mechanism whereby S421-P could increase Htt flux through the proteasome.

Indeed, S421 is a highly conserved consensus Akt phosphorylation site, and Akt is centrally involved in signaling cascades that regulate protein turnover (85). Further, S421 is situated in a region of Htt especially rich in PTMs (24), offering the possibility that one or more of these PTMs regulates Htt catabolism. Of particular note, acetylation of Htt at K444 has been reported to target Htt to autophagosomes for degradation (38), whereas our work suggests that S421-P might increase Htt flux through the proteasome. An enticing hypothesis, therefore, is that regulation of these two relatively nearby PTMs determines whether Htt is degraded by the proteasome or by autophagy, the two main pathways of turnover for cytosolic proteins (86). Considering that mHtt causes impaired loading of autophagosomes (87), its targeting to the proteasome might be crucial for preventing neuronal dysfunction and death. Indeed, a neuron's ability to turn over mHtt can be a greater determinant of toxicity than overall mHtt levels (A.T. and S.F., unpublished data). In this scenario, the decrease of S421-P caused by polyQ expansion could be considered a toxic LOF that is prevented by phosphomimetic S421D mutation. Recently, it was found that serines 431 and 432 of Htt are also phosphorylation sites whose mutation can influence mHtt accumulation and that K444 can be ubiquitinated in addition to being acetylated (41). These findings further support the hypothesis that PTMs in this region of Htt are crucial regulators of Htt clearance. Finally, the age-

dependent decline in proteasome function (88) and consequent inability to process the same levels of flux could explain why the S421D mice finally developed rotarod deficits at 12 months of age.

Why were the ameliorating effects of S421D most apparent in the striatum? Circuit-specific factors, such as the predominance of inhibitory GABAergic MSNs (89), likely play a role. Additionally, MSNs are dependent on other brain regions for the delivery of a critical extracellular growth factor, BDNF (13), whose downstream effects include activation of Akt. While we did not detect significantly decreased *BDNF* transcription, small changes unable to be detected by our techniques could still play a role, especially over the course of a progressive disease. These and other factors likely explain why, under normal conditions, the striatum shows less phosphorylation at S421 than do other brain regions less affected in HD (50). This implies that the S421D mutation represents a particularly consequential change to this brain region. Additionally, the striatal expression profile likely modulates the effect of S421D. For example, the Ras homologue Rhes is highly enriched in the striatum where it sumoylates mHtt, greatly enhancing its toxicity (39). Intriguingly, sumoylation competes with and thereby decreases ubiquitination of lysines, leading to an increase in soluble levels of mHtt (25). The apparent increase in mHtt flux through the proteasome caused by S421D might counteract this process. Yet it is also worth noting that S421D might decrease steady-state levels of mHtt in brain regions beyond the striatum, but western blots of brain lysates and qRT-PCR may not be sufficiently sensitive to detect a more modest effect. For example, comparison of the S421D line to BACHD mice revealed a trend towards increased cortical levels of mHtt mRNA with no such trend noted at the protein level, consistent with the possibility that S421D might increase mHtt turnover in the cortex as well.

Of note, 4H7H7 staining was down by 30% by IHC (where proteins are fixed in their native conformation) but total Htt levels were down by only 15% by western blot (where proteins are denatured). While there are considerable limitations to the quantification, particularly in the case of IHC, this discrepancy could be revealing. Recently, it has been shown that disease-associated polyQ stretches can adopt a compact hairpin structure (90) *in situ*, whose presence quantitatively and significantly predicts neurodegeneration (91). This structure is recognized by mAb 4H7H7 (J.M., S.F., unpublished data). Hence, the aforementioned discrepancy could mean that S421 regulates Htt conformation directly or that the fraction of Htt that is lowered in the striatum has particularly adopted the compact hairpin structure recognized by mAb 4H7H7. Since this conformation predicts toxicity, neurons might be accelerating the clearance of this subset of Htt molecules in order to enhance their survival.

There are presumably several other mechanisms that play an important role in orchestrating S421D's ability to diminish mHtt toxicity. Although we did not detect *BDNF* transcriptional deficits, for example, mHtt has also been reported to decrease anterograde transport of BDNF in cortical neurons (79), which is critical for its delivery to the striatum. Further, S421-P has been reported to restore this mHtt-induced vesicular trafficking defect (46), potentially allowing the use of the S421D mice to confirm these findings. However, such cortical trafficking deficits have been controversial (92) and have not been reported in BACHD mice, limiting our ability to test this hypothesis in the S421D mice. It is worth nothing, however, that while our immunohistochemistry for BDNF in BACHD mice did not detect overall changes in BDNF levels, we did note some changes in BDNF accumulation, which could be consistent with a heretofore undescribed trafficking deficit in the BACHD model.

Although previous reports have observed *BDNF* and REST-mediated transcriptional dysfunction in the setting of mHtt, we did not detect any such changes. The explanations behind this discrepancy remain unclear, but one possibility is that transcriptional dysfunction is a late event in HD that is more easily appreciated in the context of aggressive models based on the expression of N-terminal mHtt fragments. Another possibility is that the presence of diploid, endogenous mouse *Htt* is able to compensate for this particular deficit caused by the transgenic mHtt. In principle, the mice produced by transgenic rescue of endogenous *Htt* knockout could address the latter possibility, but the burden of the breeding necessary to obtain a cohort of these mice (1 of 7 expected rescue mice) makes the logistics of such an experiment difficult. Finally, small procedural differences from the previously published studies might explain our discordant results, particularly when studying a molecule as potentially labile as RNA.

How do our results fit with current models of polyQ disease? Increasing evidence suggests that, as opposed to the conventional view, polyQ diseases might instead be explained by a dominant GOF together with a role for LOF (Fig. 16) (93-95). In the wild-type setting, the host protein might adopt one of several conformations, depending on specific post-translational modifications, such as phosphorylation. Different conformations might, in turn, be associated with particular functions. In the disease setting, polyQ expansion could stabilize certain normal conformations of the host protein at the expense of others. That is, the wild-type equilibrium of protein conformations would be disrupted so that functions associated with preferred conformations are enhanced, whereas the remainder would be deficient.

PolyQ expansions are also known to place an extra burden on a cell's protein folding machinery. Disease might also occur because the burden disrupts proper folding of

other metastable proteins, contributing to their LOF (96). However, it is possible to imagine that the burden on the chaperone system could cause disease by enhancing a normal function of the instigating polyQ protein. If certain conformations of the polyQ protein require or are recognized by chaperones, then the reduced availability of chaperones could shift the distribution of its conformers towards those that do not require chaperones (Fig. 16). The increase in the function that corresponds to that conformer would represent a GOF linked to the protein's normal function. Together, these changes might bring about cell dysfunction and eventual death.

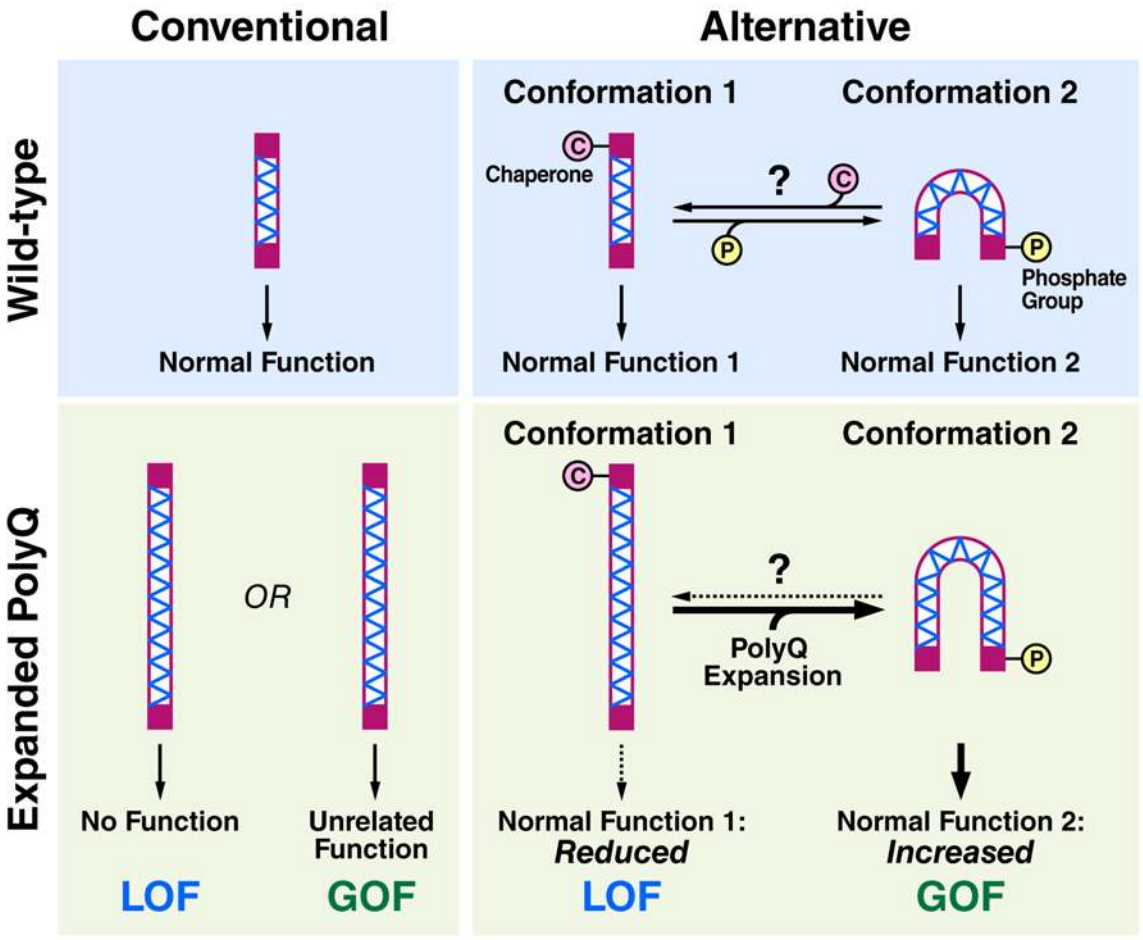

Figure 16. Conventional and alternative hypotheses on the role of an expanded

polyQ stretch in disease.

In the conventional view, a protein with a polyQ stretch (hatched region) has a specific normal function. Expansion of the polyQ stretch causes disease due to an unrelated toxic gain of function (GOF) or a loss of normal function (LOF). In an alternative view, the protein exists in an equilibrium of distinct conformations, some associated with particular and distinct normal functions. The equilibrium could be influenced in multiple ways, including chaperone binding (pink circle) and post-translational modifications, such as phosphorylation (yellow circle). With polyQ expansion, the equilibrium is disturbed, leading to GOF associated with enhanced function of the stabilized conformer. There is also LOF due to decreased function associated with the less preferred conformer. The polyQ expansion could affect the equilibrium by stabilizing one of the conformers directly or by promoting an interaction with a conformation-specific binding partner (not depicted), or indirectly by reducing chaperone availability through stress on the protein homeostasis machinery.

Our studies of S421-P are certainly consistent with a model of this sort. The potentially increased trafficking of Htt-S421D through the proteasome could represent a native Htt function enhanced either directly or indirectly by the phosphomimetic mutation. As such, S421D might counteract the toxic LOF caused by the decrease in S421-P that occurs with polyQ expansion. Additionally, S421-P might push Htt away from other conformations that are associated with GOF toxicity and/or increased stress on the protein homeostasis machinery. In sum, S421-P might restore a less toxic equilibrium of Htt conformations and associated functions, thereby ameliorating both GOF and LOF toxicity. Our ongoing studies of possible subtle changes associated with S421-P on Htt conformations, interaction partners, and subcellular localization should help validate or refine these ideas.

While discussing polyQ disease more generally, the possible broader impact of phosphorylation at Akt consensus sites is worthy of mention. For example, spinocerebellar ataxia type 1 (SCA1) is caused by a polyQ expansion in the ataxin-1 (Atxn1) protein, and like Htt, Atxn1 has an Akt consensus site at S776 that has been shown to play a crucial role in Atxn1-mediated toxicity *in vitro* and *in vivo* (81, 97). Unlike Htt, however, phosphorylation of Atxn1 at S776 is necessary for toxicity, as it enhances binding of Atxn1 to 14-3-3 proteins and thereby slows normal protein turnover. Furthermore, phosphomimetic mutation of Atxn1-S776 in the context of a non-pathogenic polyQ stretch is toxic (95), which adds support to the hypothesis that too much normal function of a polyQ protein might explain some or all of the GOF toxicity seen in polyQ disease (Fig. 16).

Why does phosphorylation of Htt-S421 and Atxn1-S776 lead to dramatically opposite effects on host protein toxicity? In fact, these results might be completely compatible. Although S776 was identified as a consensus Akt phosphorylation site, PKA instead has been identified as the active kinase *in vivo* (98). Interestingly, cerebellar Purkinje cells, which are the prominent site of pathology in SCA1, express D2 receptors (D2Rs), and D2R signaling can modulate Atxn-1 toxicity (99). The striatal MSNs of the indirect pathway also express D2Rs, and these MSNs are similarly thought to be the most vulnerable in HD (2). In both cases, the effect might be due to regulation of kinase activity, as D2R signaling *activates* PKA but *inhibits* Akt (100). Thus, D2R activation *increases* phosphorylation of Atxn1-S776 but *decreases* phosphorylation of Htt-S421, which others and we have now shown to modulate the toxicity of both mutant proteins, respectively, *in vivo*.

There is still further evidence for a modulatory role of Akt consensus sites in polyQ diseases. PolyQ expansion in the androgen receptor (AR) leads to spinal and bulbar muscular atrophy (SBMA), also referred to as Kennedy's disease (22). The AR contains two Akt consensus sites, and phosphorylation at one or both of these sites decreases AR translocation to the nucleus and blocks AR-induced apoptosis in cell culture (101). Additionally, phosphomimetic mutation at both sites substantially reduces the toxicity of polyQ-expanded AR in a motor neuron cell line (102), and overexpression of IGF-1—which is known to lead to Akt activation—in the skeletal muscle of a transgenic mouse model of SBMA significantly attenuates disease (103). IGF-1 overexpression also led to increased clearance of the mutant AR by the proteasome, a finding that could be consistent with our data suggesting that phosphorylation of Htt at S421 increases Htt flux through the proteasome. In sum, the apparent importance of Akt consensus sites to HD, SCA1, and SBMA pathogenesis suggests that it will be fascinating to determine if there are any such sites in other proteins with polymorphic polyQ expansions, and if so, whether they similarly modulate the toxicity or turnover of the host protein.

In conclusion, this study demonstrates the significance of S421 to the toxicity of fl-mHtt *in vivo*. Our findings indicate that increasing levels of S421-P in HD patients could be a viable therapeutic target for this devastating disease. Given Akt's oncogenic potential (85), direct activation may not be an optimal approach, but future work focused on the effects of S421D on mHtt's local structure and binding partners might present suitable targets for a small molecule drug.

References

1. Walker FO (2007) Huntington's disease. *Lancet* 369(9557):218-228.
2. Finkbeiner S (2011) Huntington's disease. *Cold Spring Harb. Perspect. Biol.* 3:a007476.
3. Huntington's Disease Collaborative Research Group (1993) A novel gene containing a trinucleotide repeat that is expanded and unstable on Huntington's disease chromosomes. The Huntington's Disease Collaborative Research Group. *Cell* 72(6):971-983.
4. Wexler NS*, et al.* (2004) Venezuelan kindreds reveal that genetic and environmental factors modulate Huntington's disease age of onset. *Proc. Natl. Acad. Sci. U.S.A.* 101:3498–3503.
5. Vonsattel JP & DiFiglia M (1998) Huntington disease. *Journal of neuropathology and experimental neurology* 57(5):369-384.
6. Arrasate M, Mitra S, Schweitzer ES, Segal MR, & Finkbeiner S (2004) Inclusion body formation reduces levels of mutant huntingtin and the risk of neuronal death. *Nature* 431:805–810.
7. Gil JM & Rego AC (2008) Mechanisms of neurodegeneration in Huntington's disease. *The European journal of neuroscience* 27(11):2803-2820.
8. Li S-H & Li X-J (2004) Huntingtin-protein interactions and the pathogenesis of Huntington's disease. *Trends Genet.* 20:146–154.
9. Levine MS, Cepeda C, & Andre VM (2010) Location, location, location: contrasting roles of synaptic and extrasynaptic NMDA receptors in Huntington's disease. *Neuron* 65(2):145-147.

10. Gidalevitz T, Ben-Zvi A, Ho KH, Brignull HR, & Morimoto RI (2006) Progressive disruption of cellular protein folding in models of polyglutamine diseases. *Science* 311(5766):1471–1474.

11. Cattaneo E, Zuccato C, & Tartari M (2005) Normal huntingtin function: an alternative approach to Huntington's disease. *Nature reviews. Neuroscience* 6(12):919-930.

12. Chao MV (2003) Neurotrophins and their receptors: a convergence point for many signalling pathways. *Nature reviews. Neuroscience* 4(4):299-309.

13. Altar CA*, et al.* (1997) Anterograde transport of brain-derived neurotrophic factor and its role in the brain. *Nature* 389(6653):856-860.

14. Baquet ZC, Gorski JA, & Jones KR (2004) Early striatal dendrite deficits followed by neuron loss with advanced age in the absence of anterograde cortical brain-derived neurotrophic factor. *J. Neurosci.* 24(17):4250–4258.

15. Xu B*, et al.* (2000) Cortical degeneration in the absence of neurotrophin signaling: Dendritic retraction and neuronal loss after removal of the receptor TrkB. *Neuron* 26(1):233–245.

16. Zuccato C*, et al.* (2001) Loss of huntingtin-mediated BDNF gene transcription in Huntington’s disease. *Science* 293:493–498.

17. Zuccato C & Cattaneo E (2007) Role of brain-derived neurotrophic factor in Huntington's disease. *Progress in neurobiology* 81(5-6):294-330.

18. Ferrer I, Goutan E, Marin C, Rey MJ, & Ribalta T (2000) Brain-derived neurotrophic factor in Huntington disease. *Brain research* 866(1-2):257-261.

19. Strand AD*, et al.* (2007) Expression profiling of Huntington's disease models suggests that brain-derived neurotrophic factor depletion plays a major role in striatal

degeneration. *The Journal of neuroscience : the official journal of the Society for Neuroscience* 27(43):11758-11768.

20. Borrell-Pages M, Zala D, Humbert S, & Saudou F (2006) Huntington's disease: from huntingtin function and dysfunction to therapeutic strategies. *Cellular and molecular life sciences : CMLS* 63(22):2642-2660.

21. Imarisio S*, et al.* (2008) Huntington's disease: from pathology and genetics to potential therapies. *The Biochemical journal* 412(2):191-209.

22. Orr HT & Zoghbi HY (2007) Trinucleotide repeat disorders. *Annu. Rev. Neurosci.* 30:575–621.

23. Pennuto M, Palazzolo I, & Poletti A (2009) Post-translational modifications of expanded polyglutamine proteins: impact on neurotoxicity. *Human molecular genetics* 18(R1):R40-47.

24. Ehrnhoefer DE, Sutton L, & Hayden MR (2011) Small changes, big impact: posttranslational modifications and function of huntingtin in Huntington disease. *The Neuroscientist : a review journal bringing neurobiology, neurology and psychiatry* 17(5):475-492.

25. Steffan JS*, et al.* (2004) SUMO modification of huntingtin and Huntington's disease pathology. *Science* 304:100–104.

26. Aiken CT*, et al.* (2009) Phosphorylation of threonine-3: Implications for huntingtin aggregation and neurotoxicity. *J. Biol. Chem.* 284:29427–29436.

27. Gu X*, et al.* (2009) Serines 13 and 16 are critical determinants of full-length human mutant huntingtin induced disease pathogenesis in HD mice. *Neuron* 64:828–840.

28. Thompson LM*, et al.* (2009) IKK phosphorylates Huntingtin and targets it for degradation by the proteasome and lysosome. *J. Cell Biol.* 187:1083–1099.

29. Atwal RS*, et al.* (2011) Kinase inhibitors modulate huntingtin cell localization and toxicity. *Nat. Chem. Biol.* 7(7):453–460.

30. Di Pardo A*, et al.* (2012) Ganglioside GM1 induces phosphorylation of mutant huntingtin and restores normal motor behavior in Huntington disease mice. *Proc. Natl. Acad. Sci. U.S.A.* 109(9):3528–3533.

31. Humbert S*, et al.* (2002) The IGF-1/Akt pathway is neuroprotective in Huntington's disease and involves huntingtin phosphorylation by Akt. *Dev. Cell* 3:1–20.

32. Wellington CL*, et al.* (2002) Caspase cleavage of mutant huntingtin precedes neurodegeneration in Huntington's disease. *The Journal of neuroscience : the official journal of the Society for Neuroscience* 22(18):7862-7872.

33. Luo S, Vacher C, Davies JE, & Rubinsztein DC (2005) Cdk5 phosphorylation of huntingtin reduces its cleavage by caspases: Implications for mutant huntingtin toxicity. *J. Cell Biol.* 169(4):647–656.

34. Graham RK*, et al.* (2006) Cleavage at the caspase-6 site is required for neuronal dysfunction and degeneration due to mutant huntingtin. *Cell* 125(6):1179–1191.

35. Schilling B*, et al.* (2006) Huntingtin phosphorylation sites mapped by mass spectrometry. Modulation of cleavage and toxicity. *J. Biol. Chem.* 281(33):23686–23697.

36. Yanai A*, et al.* (2006) Palmitoylation of huntingtin by HIP14 is essential for its trafficking and function. *Nat. Neurosci.* 9(6):824–831.

37. Anne SL, Saudou F, & Humbert S (2007) Phosphorylation of huntingtin by cyclin-dependent kinase 5 is induced by DNA damage and regulates wild-type and mutant huntingtin toxicity in neurons. *The Journal of neuroscience : the official journal of the Society for Neuroscience* 27(27):7318-7328.

38. Jeong H*, et al.* (2009) Acetylation targets mutant huntingtin to autophagosomes for degradation. *Cell* 137(1):60-72.

39. Subramaniam S, Sixt KM, Barrow R, & Snyder SH (2009) Rhes, a striatal specific protein, mediates mutant-huntingtin cytotoxicity. *Science* 324(5932):1327–1330.

40. Miller JP*, et al.* (2010) Matrix metalloproteinases are modifiers of huntingtin proteolysis and toxicity in Huntington's disease. *Neuron* 67(2):199-212.

41. Dong G, Callegari E, Gloeckner CJ, Ueffing M, & Wang H (2012) Mass spectrometric identification of novel posttranslational modification sites in Huntingtin. *Proteomics* 12(12):2060-2064.

42. Rangone H*, et al.* (2004) The serum- and glucocorticoid-induced kinase SGK inhibits mutant huntingtin-induced toxicity by phosphorylating serine 421 of huntingtin. *Eur. J. Neurosci.* 19(2):273–279.

43. Saudou F, Finkbeiner S, Devys D, & Greenberg ME (1998) Huntingtin acts in the nucleus to induce apoptosis, but death does not correlate with the formation of intranuclear inclusions. *Cell* 95:55–66.

44. Pardo R*, et al.* (2006) Inhibition of calcineurin by FK506 protects against polyglutamine-huntingtin toxicity through an increase of huntingtin phosphorylation at S421. *J. Neurosci.* 26(5):1635–1645.

45. Zala D*, et al.* (2008) Phosphorylation of mutant huntingtin at S421 restores anterograde and retrograde transport in neurons. *Hum. Mol. Genet.* 17(24):3837–3846.

46. Pineda JR*, et al.* (2009) Genetic and pharmacological inhibition of calcineurin corrects the BDNF transport defect in Huntington's disease. *Molecular brain* 2:33.

47. Colin E*, et al.* (2008) Huntingtin phosphorylation acts as a molecular switch for anterograde/retrograde transport in neurons. *EMBO J.* 27(15):2124–2134.

48. Warby SC*, et al.* (2009) Phosphorylation of huntingtin reduces the accumulation of its nuclear fragments. *Mol. Cell. Neurosci.* 40(2):121–127.

49. Metzler M*, et al.* (2010) Phosphorylation of Huntingtin at Ser^{421} in YAC128 neurons is associated with protection of YAC128 neurons from NMDA-mediated excitotoxicity and is modulated by PP1 and PP2A. *J. Neurosci.* 30:14318-14329.

50. Warby SC*, et al.* (2005) Huntingtin phosphorylation on serine 421 is significantly reduced in the striatum and by polyglutamine expansion *in vivo*. *Hum. Mol. Genet.* 14(11):1569–1577.

51. Wang LH & Qin ZH (2006) Animal models of Huntington's disease: implications in uncovering pathogenic mechanisms and developing therapies. *Acta pharmacologica Sinica* 27(10):1287-1302.

52. Mangiarini L*, et al.* (1996) Exon 1 of the HD gene with an expanded CAG repeat is sufficient to cause a progressive neurological phenotype in transgenic mice. *Cell* 87:493–506.

53. Heng MY*, et al.* (2010) Early autophagic response in a novel knock-in model of Huntington disease. *Human molecular genetics* 19(19):3702-3720.

54. Slow EJ*, et al.* (2003) Selective striatal neuronal loss in a YAC128 mouse model of Huntington disease. *Hum. Mol. Genet.* 12(13):1555–1567.

55. Gray M*, et al.* (2008) Full-length human mutant huntingtin with a stable polyglutamine repeat can elicit progressive and selective neuropathogenesis in BACHD mice. *J. Neurosci.* 28(24):6182–6195.

56. Graham RK*, et al.* (2006) Levels of mutant huntingtin influence the phenotypic severity of Huntington disease in YAC128 mouse models. *Neurobiol. Dis.* 21(2):444–455.

57. Miller J*, et al.* (2010) Quantitative relationships between huntingtin levels, polyglutamine length, inclusion body formation, and neuronal death provide novel insight into Huntington‘s disease molecular pathogenesis. *J. Neurosci.* 30:10541–10550.

58. Zeitlin S, Liu JP, Chapman DL, Papaioannou VE, & Efstratiadis A (1995) Increased apoptosis and early embryonic lethality in mice nullizygous for the Huntington’s disease gene homologue. *Nat. Genet.* 11(2):155–163.

59. White JK*, et al.* (1997) Huntingtin is required for neurogenesis and is not impaired by the Huntington’s disease CAG expansion. *Nat. Genet.* 17(4):404–410.

60. Hodgson JG*, et al.* (1999) A YAC mouse model for Huntington’s disease with full-length mutant huntingtin, cytoplasmic toxicity, and selective striatal neurodegeneration. *Neuron* 23:181–192.

61. Menalled L*, et al.* (2009) Systematic behavioral evaluation of Huntington's disease transgenic and knock-in mouse models. *Neurobiol. Dis.* 35(3):319–336.

62. McFadyen MP, Kusek G, Bolivar VJ, & Flaherty L (2003) Differences among eight inbred strains of mice in motor ability and motor learning on a rotorod. *Genes, brain, and behavior* 2(4):214-219.

63. Van Raamsdonk JM*, et al.* (2006) Body weight is modulated by levels of full-length huntingtin. *Human molecular genetics* 15(9):1513-1523.

64. Davies SW*, et al.* (1997) Formation of neuronal intranuclear inclusions underlies the neurological dysfunction in mice transgenic for the HD mutation. *Cell* 90(3):537–548.

65. Slow EJ*, et al.* (2005) Absence of behavioral abnormalities and neurodegeneration *in vivo* despite widespread neuronal huntingtin inclusions. *Proc. Natl. Acad. Sci. U.S.A.* 102(32):11402–11407.

66. Sathasivam K*, et al.* (2001) Centrosome disorganization in fibroblast cultures derived from R6/2 Huntington's disease (HD) transgenic mice and HD patients. *Hum. Mol. Genet.* 10:2425–2435.

67. Pouladi MA*, et al.* (2012) Marked differences in neurochemistry and aggregates despite similar behavioural and neuropathological features of Huntington disease in the full-length BACHD and YAC128 mice. *Human molecular genetics* 21(10):2219-2232.

68. Ehrlich ME*, et al.* (2001) ST14A cells have properties of a medium-size spiny neuron. *Exp. Neurol.* 167(2):215–226.

69. Gong S & Yang XW (2005) Modification of bacterial artificial chromosomes (BACs) and preparation of intact BAC DNA for generation of transgenic mice. *Current protocols in neuroscience / editorial board, Jacqueline N. Crawley ... [et al.]* Chapter 5:Unit 5 21.

70. Osmand AP, Berthelier V, & Wetzel R (2006) Imaging polyglutamine deposits in brain tissue. *Methods Enzymol.* 412:106–122.

71. Xie Y, Hayden MR, & Xu B (2010) BDNF overexpression in the forebrain rescues Huntington's disease phenotypes in YAC128 mice. *The Journal of neuroscience : the official journal of the Society for Neuroscience* 30(44):14708-14718.

72. Gharami K, Xie Y, An JJ, Tonegawa S, & Xu B (2008) Brain-derived neurotrophic factor over-expression in the forebrain ameliorates Huntington's disease phenotypes in mice. *J. Neurochem.* 105(2):369–379.

73. Canals JM*, et al.* (2004) Brain-derived neurotrophic factor regulates the onset and severity of motor dysfunction associated with enkephalinergic neuronal degeneration in Huntington's disease. *J. Neurosci.* 24(35):7727–7739.

74. Pineda JR*, et al.* (2005) Brain-derived neurotrophic factor modulates dopaminergic deficits in a transgenic mouse model of Huntington's disease. *J. Neurochem.* 93(5):1057–1068.

75. Zuccato C*, et al.* (2003) Huntingtin interacts with REST/NRSF to modulate the transcription of NRSE-controlled neuronal genes. *Nat. Genet.* 35:76–83.

76. Mortazavi A, Leeper Thompson EC, Garcia ST, Myers RM, & Wold B (2006) Comparative genomics modeling of the NRSF/REST repressor network: from single conserved sites to genome-wide repertoire. *Genome research* 16(10):1208-1221.

77. Zuccato C*, et al.* (2007) Widespread disruption of repressor element-1 silencing transcription factor/neuron-restrictive silencer factor occupancy at its target genes in Huntington's disease. *The Journal of neuroscience : the official journal of the Society for Neuroscience* 27(26):6972-6983.

78. Shimojo M (2008) Huntingtin regulates RE1-silencing transcription factor/neuron-restrictive silencer factor (REST/NRSF) nuclear trafficking indirectly through a complex with REST/NRSF-interacting LIM domain protein (RILP) and dynactin p150 Glued. *The Journal of biological chemistry* 283(50):34880-34886.

79. Gauthier LR*, et al.* (2004) Huntingtin controls neurotrophic support and survival of neurons by enhancing BDNF vesicular transport along microtubules. *Cell* 118:127–138.

80. Schoch S, Cibelli G, & Thiel G (1996) Neuron-specific gene expression of synapsin I. Major role of a negative regulatory mechanism. *The Journal of biological chemistry* 271(6):3317-3323.

81. Emamian ES*, et al.* (2003) Serine 776 of ataxin-1 is critical for polyglutamine-induced disease in *SCA1* transgenic mice. *Neuron* 38:375–387.

82. Steffan JS (2010) Does Huntingtin play a role in selective macroautophagy? *Cell Cycle* 9(17):3401-3413.

83. Zheng S*, et al.* (2010) Deletion of the huntingtin polyglutamine stretch enhances neuronal autophagy and longevity in mice. *PLoS Genet.* 6(2):e1000838.

84. Hunter T (2007) The age of crosstalk: phosphorylation, ubiquitination, and beyond. *Molecular cell* 28(5):730-738.

85. Hemmings BA & Restuccia DF (2012) PI3K-PKB/Akt pathway. *Cold Spring Harbor perspectives in biology* 4(9):a011189.

86. Wong E & Cuervo AM (2010) Integration of clearance mechanisms: the proteasome and autophagy. *Cold Spring Harbor perspectives in biology* 2(12):a006734.

87. Martinez-Vicente M*, et al.* (2010) Cargo recognition failure is responsible for inefficient autophagy in Huntington's disease. *Nature neuroscience* 13(5):567-576.

88. Keller JN, Gee J, & Ding Q (2002) The proteasome in brain aging. *Ageing research reviews* 1(2):279-293.

89. Lobo MK (2009) Molecular profiling of striatonigral and striatopallidal medium spiny neurons past, present, and future. *International review of neurobiology* 89:1-35.

90. Peters-Libeu C*, et al.* (2012) Disease-associated polyglutamine stretches in monomeric huntingtin adopt a compact structure. *J. Mol. Biol.* 421:587–600.

91. Miller J*, et al.* (2011) Identifying polyglutamine protein species *in situ* that best predict neurodegeneration. *Nat. Chem. Biol.* 7:925–934.

92. Her LS & Goldstein LS (2008) Enhanced sensitivity of striatal neurons to axonal transport defects induced by mutant huntingtin. *The Journal of neuroscience : the official journal of the Society for Neuroscience* 28(50):13662-13672.

93. Kratter IH & Finkbeiner S (2010) PolyQ disease: Too many Q's, too much function? *Neuron* 67:897–899.

94. Nedelsky NB*, et al.* (2010) Native functions of the androgen receptor are essential to pathogenesis in a Drosophila model of spinobulbar muscular atrophy. *Neuron*:936–952.

95. Duvick L*, et al.* (2010) SCA1-like disease in mice expressing wild type ataxin-1 with a serine to aspartic acid replacement at residue 776. *Neuron*:929–935.

96. Powers ET, Morimoto RI, Dillin A, Kelly JW, & Balch WE (2009) Biological and chemical approaches to diseases of proteostasis deficiency. *Annu. Rev. Biochem.* 78:959–991.

97. Chen H-K*, et al.* (2003) Interaction of Akt-phosphorylated ataxin-1 with 14-3-3 mediates neurodegeneration in spinocerebellar ataxia type 1. *Cell* 113:457–468.

98. Jorgensen ND*, et al.* (2009) Phosphorylation of ATXN1 at Ser776 in the cerebellum. *Journal of neurochemistry* 110(2):675-686.

99. Hearst SM, Lopez ME, Shao Q, Liu Y, & Vig PJ (2010) Dopamine D2 receptor signaling modulates mutant ataxin-1 S776 phosphorylation and aggregation. *Journal of neurochemistry* 114(3):706-716.

100. Beaulieu JM, Del'guidice T, Sotnikova TD, Lemasson M, & Gainetdinov RR (2011) Beyond cAMP: The Regulation of Akt and GSK3 by Dopamine Receptors. *Frontiers in molecular neuroscience* 4:38.

101. Lin HK, Yeh S, Kang HY, & Chang C (2001) Akt suppresses androgen-induced apoptosis by phosphorylating and inhibiting androgen receptor. *Proceedings of the National Academy of Sciences of the United States of America* 98(13):7200-7205.

102. Palazzolo I*, et al.* (2007) Akt blocks ligand binding and protects against expanded polyglutamine androgen receptor toxicity. *Human molecular genetics* 16(13):1593-1603.

103. Palazzolo I*, et al.* (2009) Overexpression of IGF-1 in muscle attenuates disease in a mouse model of spinal and bulbar muscular atrophy. *Neuron* 63(3):316-328.

104. Yang XW, Model P, & Heintz N (1997) Homologous recombination based modification in Escherichia coli and germline transmission in transgenic mice of a bacterial artificial chromosome. *Nat. Biotechnol.* 15(9):859–865.

105. Yang XW & Gong S (2005) An overview on the generation of BAC transgenic mice for neuroscience research. *Current protocols in neuroscience / editorial board, Jacqueline N. Crawley ... [et al.]* Chapter 5:Unit 5 20.

Appendix 1: Visualizing Intracellular Htt-S421-P

Introduction and Results

One common function of PTMs is to alter subcellular localization, and this is true in the case of Htt (28, 29, 36, 38). The majority of these findings come from model systems based on overexpression of an N-terminal fragment of Htt in cell lines, with subsequent immunocytochemistry or epifluorescence microscopy to visualize Htt localization. Conversely, subcellular fractionation of BACHD brain lysates has proven to be insufficiently sensitive to detect the modest subcellular changes associated with a change at a single PTM (27). (Of course, an alternative explanation is that the findings from cell culture do not apply to full-length Htt or full-length Htt *in vivo.*) Due to these discrepancies, we have taken several different approaches to assay whether S421-P or the S421D mutation alter Htt subcellular localization.

First, we compared 4H7H7 staining in slices from BACHD and S421D mouse striatum (Fig. 11a). There were no substantial differences, though there might have been hints of relatively decreased nuclear and increased axonal staining in the S421D slices. As a complementary method, we stained cortical and striatal slices from BACHD and S421D mice with our anti-S421-P phosphospecific antibodies (Fig. 17).

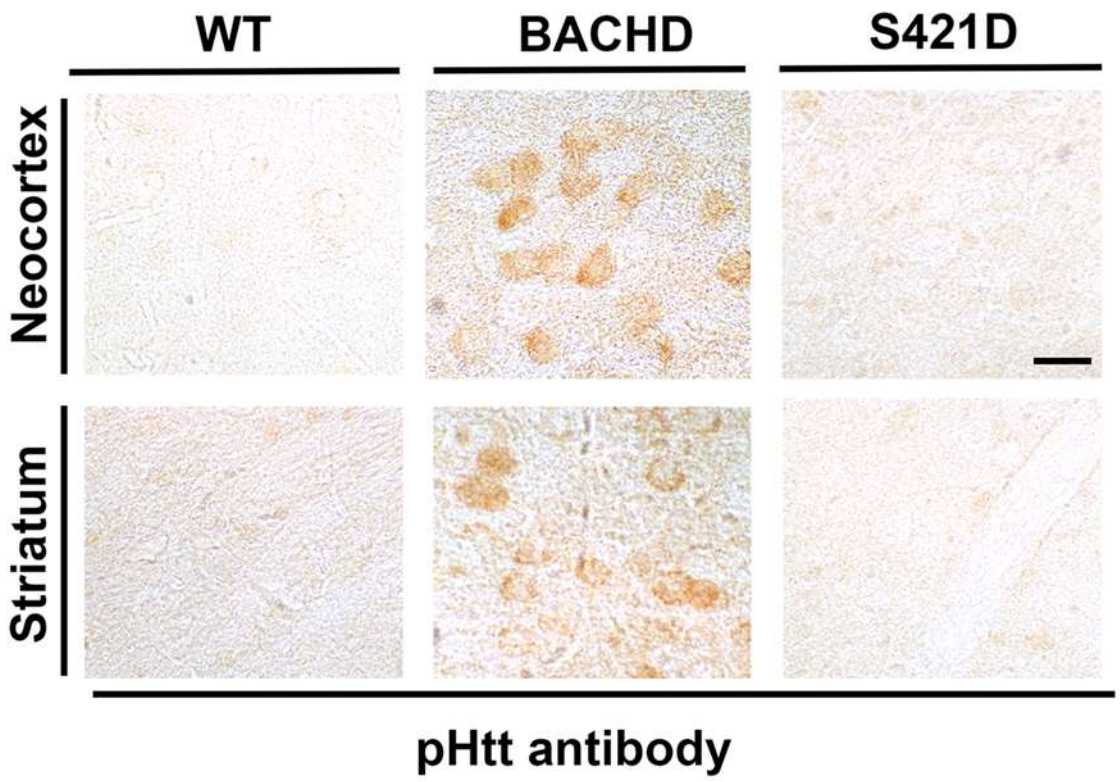

Figure 17. Immunohistochemistry with S421-P phosphospecific antibodies.

Immunohistochemical staining of cortical and striatal slices with our affinity-purified anti-S421-P phosphospecific antibodies reveals predominantly perinuclear and cytoplasmic staining. As expected, the WT control and S421D slices show no significant reactivity. The scale bar represents 20 µm.

As expected, S421D slices showed no reactivity (Fig. 1b). The S421-P signal was low in BACHD mice, also as expected, and its distribution appeared similar to the 4H7H7 staining of S421D brain slices with the exception of no clear staining of the axon. The majority of the staining was perinuclear and cytoplasmic, with the latter likely representing endoplasmic reticulum (ER) and endosomal structures.

To explore S421D subcellular localization at even higher magnification, we performed immunogold electron microscopy (EM) on cortical brain slices with 4H7H7 (Fig. 18).

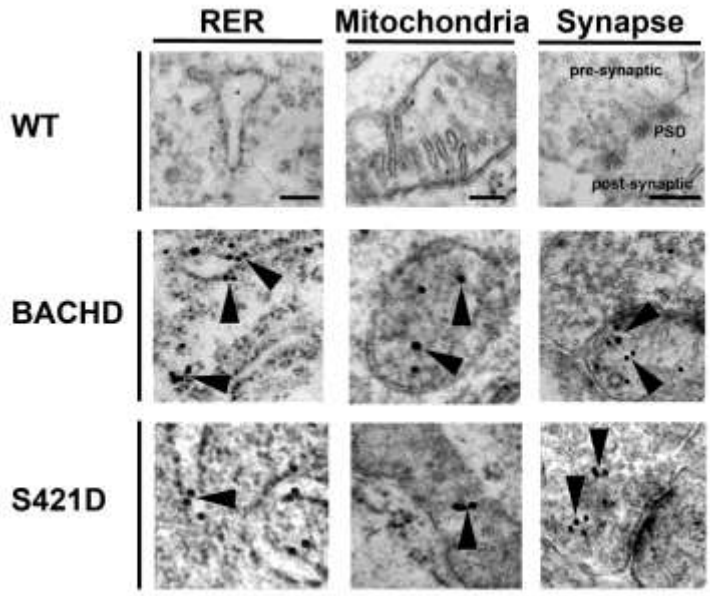

Figure 18. 4H7H7 Immunogold electron microscopy.

4H7H7 immunogold electron microscopy of cortical slices reveals mHtt localized to the rough endoplasmic reticulum (RER), mitochondrial matrix, and synapse in both BACHD and S421D mice. Intriguingly, the mHtt in BACHD mice is preferentially post-synaptic, whereas in S421D mice it is preferentially pre-synaptic. The scale bars represent 100 nm for both the RER and mitochondria and 500 nm for the synapse.

As expected, mHtt localized to the rough ER, mitochondrial matrix, and synaptic regions. The most obvious difference was a preferential post-synaptic localization of mHtt in BACHD mice but a preferential pre-synaptic localization of mHtt in the S421D mice. This could be consistent with a rescue of putative mHtt-induced anterograde vesicular trafficking deficits by phosphomimetic mutation at S421 (45). Alternatively, the synaptic

mHtt might be associated with smooth ER, but it is difficult to be certain from these images alone.

Finally, given the success other groups have had using N-terminal fragments of Htt to ascertain changes in subcellular localization with PTM, we transfected Htt-N586 constructs into N2a cells and visualized them 24 hours later using confocal microscopy (Fig. 19a). There were no obvious differences in subcellular localization evoked by the S421 mutations. We performed a similar study in mouse primary cortical neurons. Careful analysis revealed a trend towards a decreased nuclear to cytoplasmic ratio in the S421D versus S421 condition (Fig. 19b). However, further study is needed to determine if the trend represents normal variation or a significant difference.

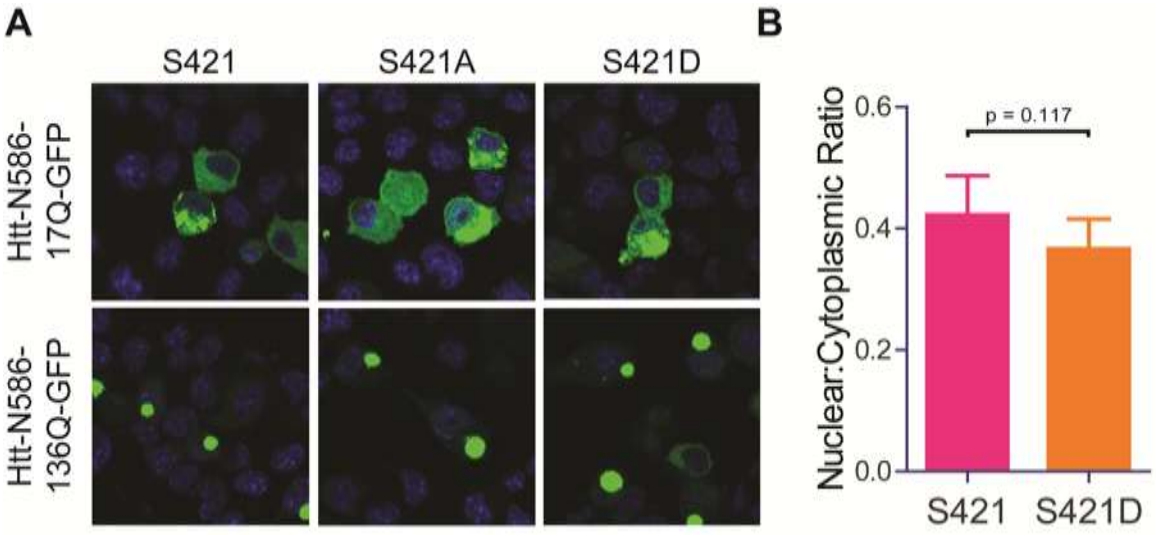

Figure 19. Subcellular localization of Htt-N586.

(A) N2a cells were transfected with different versions of Htt-N586-GFP and visualized 24 hours later by confocal microscopy after Hoechst staining. There were no obvious changes in subcellular distribution.

(B) Primary cortical neurons were transfected with Htt-N586-17Q-GFP or Htt-N586-17Q-

GFP-S421D and fixed 48 h later. Average nuclear and cytosplasmic intensities were tabulated blinded to genotype and a ratio was calculated after background subtraction. S421D showed a trend towards a subtle decrease in nuclear localization. The Mann-Whitney test was used to compare the means so as not to assume a Gaussian distribution of the data. Error bars depict the mean ± 95% confidence interval.

Methods

Immunohistochemistry. Brain slices were stained using our affinity purified rabbit anti Htt-S421-P phosphospecific antibodies with the same protocol as described in chapter 2 of this thesis.

Immunogold labeling and electron microscopy. Brain slices were prepared as described for immunohistochemistry. The immunogold labeling and electron microscopy were performed as previously published (91).

Immunocytochemistry. Mouse primary cortical neurons were plated on coverslips and co-transfected with eGFP-tagged human Htt-N586-136Q or Htt-N586-136Q-S421D and mApple as a transfection marker. Cultures were fixed 24 h later with 4% PFA, permeabilized with 0.1% Triton-X, blocked, immunolabeled overnight with 3B5H10 antibody, and finally labeled with cy5-conjugated goat anti-mouse secondary. Images were captured using a 63X, 1.4 N.A. oil immersion lens on a Confocal Zeiss LSM 510 microscope. Each neuron subjected to quantitative fluorescent imaging was selected randomly using the mApple channel and focused on using the fast-focus option of the lsm software using the DAPI channel. For each cell, images for DAPI, GFP, mApple, and Cy5 were acquired using the appropriate filters. The photomultiplier tube

(PMT) detector gain and offset settings were dictated by the detection range necessary to image each channel, with a single consistent setting used for each channel across all constructs. Images were analyzed with ImageJ (NIH) in a blinded fashion. Only neurons that appeared healthy were analyzed. For each neuron, mean intensities of a circular region of interest drawn over the nucleus, a representative region of the cytoplasm, and the local background signal were collected. Both nuclear and cytoplasmic signal intensities were corrected for the local background signal and then a ratio was calculated.

Appendix 2: BAC DNA Purification for Microinjection

This protocol for the purification of high molecular weight (HMW) BACs for subsequent microinjection into mouse embryos is adopted and modified from several different sources: the original protocols published by Prof. X. William Yang and collaborators (69, 104, 105), modifications taught by Dr. Xiaofeng Gu of the Yang laboratory during a visit to UCLA, the University of Michigan Transgenic Core (http://www.med.umich.edu/tamc/bacdna.html), and a protocol from the lab of Prof. Douglas Mortlock (http://labnodes.vanderbilt.edu/resource/view/id/1121). PFGE protocol adopted and modified from Dr. Edward Hsiao. Steps have been optimized for equipment at the Gladstone Institutes of Neurological Disease and for purification of a ~240kb BAC containing a long CAG-CAA repeat stretch.

General notes: All centrifugation steps are performed at 4° C unless otherwise noted. Use autoclaved solutions if possible and DNase free tips and tools when necessary. Always gently pour or use cut tips when handling DNA and at any step beyond bacterial lysis. For DNA dissolving steps, it is almost always worthwhile to place the tube in a 37 water bath for 5-15 min before proceeding to the next step. Otherwise, try to keep everything on ice unless otherwise stated. Use a swinging bucket rotor whenever possible (JS13.1 for Finkbeiner lab) so that small pellets can be more easily located. Every step has to be done very gently!! For example, this means no inversion of tubes but instead you gently swirl or slowly lay the tube on its side and then slowly roll it. The goal is to be very gentle but also efficient so that the DNA is not handled any more than necessary, as it is very fragile and every step increases the likelihood of sheering. Always remember to balance your tubes before spinning with the appropriate reagent!

Day One:

1. Streak out the bacteria containing the BAC from your glycerol stock onto a plate with appropriate antibiotic resistance (often chloramphenicol), being sure to use appropriate technique such as to isolate single colonies. Incubate the plate overnight at 30° C. The 30° is especially important for BACs with long repeat stretches, but is worth doing in general since replication errors will occur at a lower frequency, a highly desirable outcome when the DNA will be used to generate a mouse line.

Day Two:

1. Inoculate a single colony into 4 ml of LB with antibiotic and grow again at 30° C overnight. Do this for several colonies.

Day Three:

1. Transfer the overnight culture into 700 ml LB medium with antibiotic and culture overnight at 30° C.

Day Four:

1. Harvest the bacteria early the next morning. The OD600 should be ~1.2. Make sure to keep your OD readings in the linear range when measuring, as it is important not to overgrow the cultures.
2. Split the 700 ml culture into two standard 500ml tubes. Use the F10 rotor and spin at 6000 x g for 15 min. Carefully discard the supernatant.

3. Re-suspend the pellet (without vortexing) with 25 ml ice-cold NaCl solution (use 0.1ml of 5M NaCl solution per 50ml ddH2O). Spin at 6000 x g for 15 min.
4. Immediately (this pellet is not as solid as the previous one and you want to preserve as much starting material as possible) and gently pour off the supernatant. Freeze the pellet at -80° C overnight (or for at least 2 hours).

Day Five:

1. Place solutions I and III on ice.
2. Thaw the pellet at room temperature (~20 min). Slowly add 5 ml ice-cold solution I and mix thoroughly. Do not vortex to resuspend. Recombine the two pellets into one tube (total 10 ml) before proceeding. If your pellets were quite large then you might choose not to combine, but I found that insufficient starting material was a major problem in terms of actually recovering enough BAC by the end of the protocol. However much solution you use, keep the following ratios constant and as you proceed ensure that you've added enough solution to resuspend, lyse, and neutralize all bacteria. It is very important to add solutions II and III quite slowly without exceeding the 5 min lysing time, so do not try to do more than two tubes at a time for steps 2-4.
3. Add 20 ml of fresh solution II very gently by adding it around the rim of the tube slowly while gently swirling the tube. Mix the tube gently by rolling at room temperature for not more than 5 min.
4. Slowly add 15 ml ice-cold solution III very gently and mix thoroughly and gently.
5. Place on ice for 30 min, with a gentle mix every 10 min. More than 30 min on ice is not a problem if you have more tubes from the previous steps that need to catch up to this step.

6. Spin in the F10 at 10,000 rpm for 20 min at 4 C. If you need to add solution to balance the tubes, use solution I. During the spin, pre-chill 50 ml tubes for the JS 13.1 rotor (you might need more than one per 500 ml tube).
7. Immediately at the end of the spin, gently pour the supernatant into a new pre-chilled 50 ml tube. The bacterial debris does not pellet very well, so be careful. Most of the time, despite your best effort, some of the debris will end up in the 50 ml tube, and this is okay. Just try and not to let a significant portion to transfer. Even if it does, you'll be able to remove it at the next step, but it will take more 50 ml tubes.
8. Spin the 50ml tubes in the JS 13.1 rotor at 10,000 rpm for 15 min at 4° C. Prepare for the next step during the spin.
9. Immediately and gently pour the supernatant through a cell strainer (BD Falcon, 70 µm or 100 µm) into a 50 ml tube that is on ice. Try to minimize shearing forces associated with the filtering into the tube. Go slowly, as any small bit of debris rapidly clogs the strainer and results in spillage. Have multiple filters ready per tube just in case.
10. Transfer the supernatant back into a pre-chilled 500 ml tube.
11. Add an equal volume (~45 ml) of room temperature molecular biology grade isopropanol slowly by tilting the tube and rotating it as you add. Mix thoroughly and gently by rolling the tube on its side for ~2 min but do not invert.
12. 10,000 rpm X 20 min at 4° C in the F10. Immediately but very carefully discard the supernatant. There should be a long, spread-out pellet on one "side" of the tube. Invert and let dry at RT for ~1 min.
13. Add 9 ml TE buffer to dissolve the pellet. Add it slowly and do not pipet up and down at any point, just swirl gently and/or leave the tube on its side for a couple

of minutes. A few minutes of time in the 37° C water bath also can be helpful here.

14. Transfer to a 30 ml tube.
15. Add 4.5 ml 7.5 M K-acetate, mix gently.
16. Place at -80° C for 30 min.
17. Thaw completely at room temp (~20 min). Then spin at 6000 rpm X 10 min at 4° C in the JS 13.1.
18. Transfer the supernatant into 50 ml tubes. You will need to divide one tube into two 50 ml tubes; or, more ideally, divide 2 tubes into 3 tubes. (It's worth combining different preps to ensure sufficient material unless you're concerned about one of them.) Add 2.5 volumes of ice-cold molecular biology grade 100% ethanol. Mix thoroughly and gently by slowly rolling the tube on its side for several minutes. With the 50 ml tubes, either keep them at a slight tilt or wrap parafilm around the cap to prevent leakage.
19. Spin in the JS 13.1 at 13000 rpm X 30 min. Carefully discard the supernatant by decanting, and use a pipette if needed to get the vast majority of the supernatant out.

At this point there are two options. You can proceed with a phenol/chloroform extraction or you can instead do two successive rounds of CsCl spins. I prefer the latter approach if you have the time (takes an extra day) since it reduces handling of the DNA and allows you to avoid dealing with phenol and chloroform. However, the extraction step also works fine and saves you a day, though it does make this day longer. If you want to do the extraction, continue working here. If not, then proceed to step 4 on day six.

20. Gently add a combined sum of 8 ml TE buffer to the tubes that represent one prep to completely dissolve the pellets. For example, if in step 18 you divided two tubes into three, the DNA in those three tubes should be dissolved and combined in a total of 8 ml TE. Make sure to use polystyrene tubes at this step (the 50 ml JS 13.1 tubes work, the 30 ml ones do not), which can withstand the phenol/chloroform.
21. Add 2ml Phenol per tube (avoid the thin tris layer in the phenol). Work in the fume hood and keep all phenol related waste separate for hazardous material disposal. Mix completely and gently by slowly rolling for several minutes. If you're using the 50 ml tubes, again use parafilm and an angle to prevent leaking near the cap.
22. Add 2 ml Chloroform per tube, mix again for several minutes
23. Use the JS 13.1 to spin the tubes at 13000 rpm for 30 min.
24. Use cut tips to transfer the supernatant (top layer, ~4 mL) to new 30 ml tubes for the JS 13.1. Begin with a cut P1000 tip and then use a cut P200 tip when near the interface.
25. Add 1:10 by volume (~0.4 ml) 3M Na-acetate and 2.4 volume (~10 mL) of ice-cold 100% molecular biology grade ethanol. Mix gently and completely.
26. Place at -20° C overnight without disturbance, or at least for 2 hours.

Day Six:

1. Reserve the ultra centrifuge. I usually use the one on the 5th floor (GIVI) since the GIND one often has errors on long runs unrelated to you.
2. Take out the mix, which should have stayed liquid.
3. Balance the tubes with ice-cold 100% molecular biology grade ethanol. 13000 rpm X 30 min in the JS 13.1. Discard the supernatant

4. Add 2 ml TE to each tube to dissolve the pellet and swirl very gently. Use the 37° C water bath if necessary.
5. Prepare for the CsCl gradient. Use 1 tube CsCl per two 30 mL tubes (so you will be combining 4 ml of TE containing DNA to 4 ml of TE with CsCl). Make up an extra tube of CsCl solution to have excess available for balancing. Dissolve 9.27 g CsCl in a new 15 mL tube with 4 mL TE and mix/warm it until more than half of CsCl is in solution.
6. Gently add 4ml of DNA (2 x 2 ml in TE) to the CsCl solution. Gently mix/warm until the CsCl is completely dissolved.
7. Add 400 µl ethidium bromide (10 mg/ml) and mix gently by rolling. From this point forward, try to keep the tubes relatively protected from light when possible until the EB is removed.
8. Gently transfer the solution with a cut tip into a Beckman OptiSeal Centrifuge Tube for rotor 70.1 Ti until full. This should be about 4 ml, and be sure to remove all air bubbles by gently squeezing. Seal the tubes using the caps provided. Label the tubes in several places.
9. Take the 70.1 Ti rotor and load the tubes, being sure to use the redesigned tube spacers which allow the tube to fit properly in the rotor. These are reusable and should be kept stored with the tubes.
10. The completely filled tubes should already be balanced, but it's worth checking. Use the blank CsCl you prepared to equilibrate the tubes if a balance pair differs in weight more than 0.10 g.
11. Spin the tubes at 65000 rpm overnight (at least 16 hr) using the Ti 70.1 at 18° C. Use 'no brake' for the deceleration. Do not cool tubes below 18° C or the CsCl will precipitate out of solution.

Day Seven:

1. Carefully bring the rotor to the chemical room (or appropriate setting), trying not to disturb the bands. Ask someone to open doors for you, etc.
2. Remove the first tube from the rotor. Use a ring stand with clamp to hold the tube tightly for you. Use a 21-gauge needle to poke a hole on top of the tube to release air. Setup a long-wave UV lamp to help visualize the band. Use appropriate PPE to protect against UV burns on the hands, arms, and face. Use a clean 18-guage needle attached to a 1 ml syringe to pierce the tube carefully just below (~0.5 cm) the EB band. If there are two bands, choose the lowest one even if it is less abundant. Be careful when inserting the needle. There is a little barb just behind the beveled point, so when you apply more pressure the needle can suddenly break through and disturb the gradient. Instead, twist the syringe back and forth while applying a gentle pressure until you softly get passed the barb.
3. Slowly extract the band into the syringe. A good pull leaves some band behind, so avoid too much solution. Somewhere between 100-500 µl is normal. Transfer the solution into a 15 ml tube, being sure to remove the needle before pushing the solution back out of the syringe.
4. Repeat for each tube, keeping all tubes protected from light while not working with them.

If you skipped the phenol/chloroform extraction, bring the volume in each tube to 4 ml with TE and return to day 5, step 5 for another round of CsCl gradient purification. If you did do the extraction or if you have now completed two rounds of spins with the ultracentrifuge, continue below.

5. Bring the volume to 2 ml by adding TE buffer.
6. Add 1 ml NaCl-saturated butanol (top layer), mix very gently by rolling, let sit for 30 sec for separation, and remove and discard the top layer containing EB appropriately. Use a cut P1000 tip at this step and always leave a little of the butanol layer remaining until your final removal step.
7. Repeat this extraction one time beyond the last sign of any pink color remaining in the top layer. This will be at least 5 rounds. On the final round make sure to remove all of the butanol. A cut P200 tip is more precise for the final removal.
8. Bring the total volume to 3 ml with nuclease-free H2O. Transfer to a 30 ml JS 13.1 centrifuge tube and add 9 ml 100% molecular biology grade ethanol. Mix gently and completely by rolling.
9. Place the tubes at -20° C for 30 min or overnight.
10. Spin in the JS 13.1 at 13000 rpm for 30 min. Carefully decant away the supernatant and pipette out any remaining supernatant.
11. Add 0.5 ml of 0.3 M Na-acetate to dissolve the pellet, if any. It is not uncommon to see no pellet at this stage, which is why it's crucial to use the swinging bucket rotor. Again, a few minutes in the 37° C water bath is a good idea here.
12. Pour into standard 1.7 ml eppendorf tube and add 1ml 100% molecular biology grade ethanol, and mix gently by rocking. Avoid shearing forces.
13. Spin at 13000 rpm for 30min at 4 ° C. Make sure to orient all of the tubes so you know where to expect the pellet. A good technique is always to have the tube hinge pointed outwards. You should see a tiny, glassy pellet at this stage. Decant out the ethanol.
14. Wash with 1 ml of 70% ethanol 3 times at 13000 rpm for 3 minutes at room temperature. Make sure to use a centrifuge that doesn't heat up too much. Each

time, carefully remove the supernatant with a P1000 being very careful not to disturb the pellet. The pellet should be more visible in 70% ethanol than it was in 100% ethanol.

15. Use a pipette to remove the remaining supernatant and a kim wipe to get any small drops on the side of the tube. Allow DNA to air dry for ~2 min, but do not allow it to become completely dry.
16. Dissolve pellet using 20-40 ul microinjection buffer, depending on pellet size.
17. Allow to dissolve at 37° C for 1 hr.
18. Store DNA at 4° C.

At this point run pulsed-field gel electrophoresis (PFGE) to determine which samples look to have good concentration and minimal degregation. A tiny bit of smear is okay since the eventual dialysis will help remove it. You'll want to inject the DNA within two weeks of purification. If you have a lot of DNA but it is not clean enough, you can try another round of CsCl gradient purification. Return to day 6, step 5 to try this.

<u>Pulsed-field Gel Electrophoresis aka CHEF</u>

1. Make up 2.5 liters of 0.5X TBE running buffer.
2. Pour at least 2 liters of 0.5X TBE buffer into chamber. Make sure there is enough buffer to completely cover the pump inlet and outlet.
3. Turn on the power supply, pump, and chiller. The chiller takes a minute to turn on.

4. Set chiller to 14° C and set the timer to 1 hr. After setting the time and the temperature, have the chiller display the actual temperature. It will begin to chill (makes more noise and shows red light) a few minutes after the timer is set.
5. Pour a 1% agarose gel with NO ethidium bromide using the special casting tray with the metal comb. Make sure the metal plate is seated flat and inserted into the groves of the end plates.
6. Once the gel is solidified, remove the comb and the outer tray. Use paper towels to remove all of the excess agarose on the bottom of the black tray and the spaghetti-like strands on the sides of the gel. If not removed, this agarose can plug the pump.
7. Before submerging the gel, load your high molecular weight markers using the syringe. A forceps and spatula can be helpful here. I usually load two lanes of ladder, one with more than 0.5 cm of agarose and one with less.
8. Once the buffer is at the desired temperature, turn off the chiller first and then the pump. The system will freeze if the chiller runs without the pump.
9. Place gel in running apparatus, seated in the center of the chamber, and load liquid samples carefully. Use 5-8 µl of your DNA; you will only need a few hundred ng of DNA for eventual injection. Make samples using standard 6x DNA loading buffer, but use at a higher concentration, like 2-3X to ensure that the thick BAC DNA falls into the well. Only handle the DNA with DNase-free cut tips.
10. Load a 1kb DNA ladder. Also run a lambda standard of known concentration at various concentrations for comparing to your sample, as the nanodrop tends to be quite inaccurate for BACs.
11. The pump speed should be set between the 65 and the 70. One potential problem is that the gel can float away overnight during the run. To prevent this, use a couple of P2 tips wedged in between the gel tray and the apparatus ridge

at the bottom of the gel. (Note: buffer flows from top to bottom.) This can be tricky but is worth doing.

12. Set Block 1 with following running conditions:

    Block 1:

    6V/cm,

    120 degree angle,

    initial switch time 5 s,

    final switch time 15 s

    Time=18 hr

    Block 2:

    (holding, low voltage to prevent diffusion)

    1V/cm,

    120 degree angle,

    initial switch time 0.1s,

    final switch time 40sec (linear)

    Time=9 hrs

13. Start the run. (Note: after starting the run, you can stop the run by holding down the start/stop button until the display shows “Off”. Or, pause the program by just pressing the stop button once, which allows the resumption of an in-progress program when ready.) The current should be 140-200 mA.
14. After 15 min, turn on the pump and chiller. (The delay is to prevent any washout of the sample). Set the chiller timer at a safe amount of time. The door to the

chemical room must remain open overnight while running otherwise the pump will overheat. Post signs on the door to make sure nobody closes it.

15. After the run is completed, stain the gel with 0.5X TBE with EB or safe DNA stain for 30 min. De-stain in deionized water for 15-60 min.
16. Image the gel.
17. If you're not using the CHEF for at least 24 hours, drain the buffer. If collected, the buffer can be re-used for a run one time. When completely done with the machine, add 3 L deionized water and run the pump for a few minutes to remove the salt.
18. After draining wash water, leave the lid open for 24 hr to allow drying.

Preparing DNA for injection

Note: Although linearization of a BAC is not necessary before injection, our anecdotal experience and the experience of the Yang lab is that it improves efficiency of transgene integration.

1. Digest clean BAC DNA with 2 µl PI-Sce I enzyme, 5 µl of 10x buffer, and nuclease-free water to 50 µl at 37° C for at least 3 hours or overnight.

Dialyze digested (or undigested) DNA:

1. Fill 10 cm petri dish half-way with sterile injection buffer.
2. Put dialysis membrane on top (Millipore MF membranes 0.025 um vswp filters, cat# VSWP02500), shiny side up.
3. Drop the DNA on top with a cut tip. Cover the dish and then wrap with aluminum foil. Let salt dialyze across for at least 6 hr at room temperature.

4. Retrieve the DNA with a cut tip and store at 4 degrees. The volume recovered will be a bit smaller than the volume originally dialyzed.

At this point, run another PFGE as above. The DNA should be very clean and free from smaller fragments or streaks. Note that the BAC will run at a lower apparent size after linearization. If the DNA looks

Preparation and Solutions

All reagents should be filtered, autoclaved, or molecular biology grade as appropriate. Use autoclaved for DNase-free water. Stir bars also should be autoclaved in bottle before use.

- P1 (plus RNase), P2, P3 solutions (from Qiagen)
    - If you have brand new solutions then these are fine to use. If not, consider making your own solutions fresh (see below). This is most important for solution II, which either needs to be an un-opened Qiagen P2 or a freshly-made solution.
        - Solution I: 50 mM Glucose, 25 mM Tris pH 8.0, 10 mM EDTA, RNase A 50 µg/ml; filter sterilize and store at 4° C
        - Solution II: 0.2 M NaOH, 1% SDS; make fresh each time
        - Solution III: 50 ml of 7.5 M K-Acetate, 23 ml of glacial acetic acid, water to 200 ml; filter sterilize and store at 4° C
- 5 M NaCl

- 7.5 M K-Acetate
- 100% ethanol
- Phenol (Sigma P4557), stored at 4° C
- Chloroform (Sigma 472476)
- Isopropanol
- Ethidium bromide (10 mg/ml – the usual stock concentration)
- Cesium Chloride (Sigma C3032)
- TE: 1 ml of 1M Tris, 1 ml of 0.5M EDTA (pH 8.0), 98 ml H2O, Autoclaved
    - Or purchase fresh TE. Use pH 8.0
- NaCl-saturated Butanol: Prepare and use in fume hood. In autoclaved 250 ml bottle with stir bar, add 35 g NaCl to 100 ml TE. Stir 15 min at room temperature (not all NaCl will dissolve). Add 100 ml n-butanol (Sigma B7906), and stir vigorously for 1 hr. Allow at least 2 hours for separation before use. Store with other alcohols.
- Microinjection buffer: 10 ml of 5 M NaCl, 5 ml of 1 M Tris (pH 7.5), 100 ul of 0.5 M EDTA (pH 8.0) in 485 ml Embryo water (Sigma W1503), filter with a 0.45 um filter system

Publishing Agreement

It is the policy of the University to encourage the distribution of all theses, dissertations, and manuscripts. Copies of all UCSF theses, dissertations, and manuscripts will be routed to the library via the Graduate Division. The library will make all theses, dissertations, and manuscripts accessible to the public and will preserve these to the best of their abilities, in perpetuity.

I hereby grant permission to the Graduate Division of the University of California, San Francisco to release copies of my thesis, dissertation, or manuscript to the Campus Library to provide access and preservation, in whole or in part, in perpetuity.

Author Signature

03/20/2013

Date